Z. Phys. C - Particles and Fields 53, 51-71 (1992)

Zeitschrift für Physik C Particles and Fields

Nucleon structure functions from high energy neutrino interactions

E. Oltman[1], P. Auchincloss[2], R.E. Blair[3], C. Haber[1], S.R. Mishra[4], M. Ruiz[5], F.J. Sciulli, M.H. Shaevitz, W.H. Smith[6]
Columbia University, New York, NY 10027, USA

F.S. Merritt, M.J. Oreglia, P.G. Reutens[7]
University of Chicago, Chicago, IL 60637, USA

R. Coleman, H.E. Fis, D. Levinthal[8], W. Marsh, P.A. Rapidis, H.B. White, D. Yovanovitch
Fermi National Accelerator Laboratory, Batavia, IL 60510, USA

A. Bodek, F. Borcherding[9], N. Giokaris[10], K. Lang[11], I.E. Stockdale[12]
University of Rochester, Rochester, NY 14627, USA

Received 10 June 1991

Abstract. Structure functions obtained from high energy neutrino and antineutrino scattering from an iron target are presented. These were extracted from the combined data of Fermilab experiments E616 and E701; these utilized narrow band beam runs between 1979-1982. The structure functions are used to test the validity of quark-parton model (QPM) predictions and to extract the QCD scale parameter Λ from fits to the Altarelli-Parisi equations.

1 Introduction

Deep inelastic lepton scattering experiments offer a unique opportunity to probe nucleon structure. The differential cross sections for the charged current neutrino and antineutrino scattering by a nucleon target,

$$\begin{aligned} &\nu_\mu + N \to \mu^- + \text{hadrons} \\ &\bar{\nu}_\mu + N \to \mu^+ + \text{hadrons} \end{aligned} \tag{1}$$

are specified by the V-A structure of the charged weak current:

$$\frac{d^2\sigma^{\nu(\bar{\nu})}}{dx\,dy} = \frac{G_F^2 ME}{\pi}\left[\frac{y^2}{2}\,2xF_1 + \left(1-y-\frac{Mxy}{2E}\right)F_2 \pm y\left(1-\frac{y}{2}\right)xF_3\right]. \tag{2}$$

Here G_F is the weak coupling constant of the Fermi theory, x is the Bjorken scaling variable, y is the fractional energy transferred to the hadronic vertex, and M is the nucleon energy. The above expression is valid for momentum transfers (Q^2) such that $Q^2 \ll M_W^2$. The three structure functions, $2xF_1$, F_2 and xF_3 depend only on the Lorentz invariant functions characterizing the hadronic vertex (see Fig. 1). In terms of q^α and P^α, the 4-momentum transfer and target nucleon 4-momentum respectively, the two invariants conventionally chosen are $Q^2 = -q\cdot q$ and $x = Q^2/2P\cdot q$. All kinematic quantities appearing in (2) can be expressed in terms of the three experimentally accessible quantities: the hadron shower energy, E_h, the final state muon energy, E_μ, and muon angle, θ_μ.

$$\begin{aligned} &E = E_h + E_\mu, \quad y = E_h/E \\ &x = Q^2/2ME, \\ &Q^2 = 2E(E_\mu - |\mathbf{p}_\mu|\cos\theta_\mu) - m_\mu^2. \end{aligned} \tag{3}$$

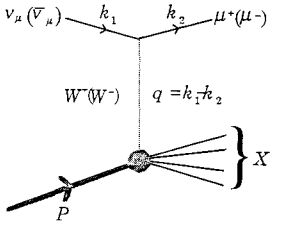

Fig. 1. Deep inelastic scattering process showing variables referenced in the text

Present addresses:
[1] LBL, Berkeley, CA 94720, USA
[2] University of Rochester, Rochester, NY 14627, USA
[3] Argonne National Laboratory, Argonne, IL 60439, USA
[4] Harvard University, Cambridge, MA 02138, USA
[5] CERN, Geneva, Switzerland
[6] University of Wisconsin, Madison, WI 53706, USA
[7] SLAC, Stanford, CA 94305, USA
[8] Florida State University, Tallahassee, FL 32306, USA
[9] Fermilab, Batavia, IL 60510, USA
[10] Rockefeller University, New York, NY 10021
[11] Stanford University, Stanford, CA 94305, USA
[12] University of Cincinnati, Cincinnati, OH 45221, USA

In the analysis presented here, the structure functions F_2 and xF_3 were extracted in x and $\log Q^2$ bins by combining the measured, energy averaged neutrino and antineutrino differential cross sections (see Sect. 3). $2xF_1$ was expressed in terms of F_2 and $R(x, Q^2) = \sigma_L/\sigma_T$, the ratio of total absorption sections for longitudinal and transverse polarized W bosons:

$$2xF_1(x, Q^2) = \frac{1 + 4M^2x^2/Q^2}{1 + R(x, Q^2)} F_2(x, Q^2). \quad (4)$$

A parametrization of R consistent with QCD predictions [1] was assumed and is shown in Appendix A.

In the quark-parton model (QPM), the nucleon constituents probed in lepton scattering experiments are the spin $-\frac{1}{2}$ quarks and antiquarks. $2xF_1$ represents the momentum fraction carried by all quarks and antiquarks. The structure function F_2 includes $2xF_1$ and any non spin-1/2 constituents, as well as effects due to quark binding. Both neutrino scattering (1) und electromagnetic scattering of charged leptons by nucleons measure these structure functions. The universality of quark-parton density states that the F_2 and $2xF_1$ measured by charged lepton beams be proportional to the same structure functions measured by neutrino beams: the proportionality constant is the mean square charge of quarks.

The structure function associated with the parity violating term in the hadronic current, xF_3, is uniquely measured in neutrino scattering. In the QPM, this structure function represents the difference between quark and antiquark momentum densities, that is, the valence quark momentum density. The Gross-Llewellyn-Smith sum rule tests this identification: the integral of xF_3/x, the valence quark number density, over all x measures the total valence quark content of the nucleon.

The observed patterns of scaling violations (Q^2 variations in structure functions) suggests an underlying dynamics of interacting quarks in the nucleon. These dynamics are studied within the context of the strong interaction theory of quantum chromodynamics (QCD) [2]. While QCD presently is unable to predict structure function values, perturbative techniques allow predictions of their evolution with Q^2.

2 Experimental setup

Pions and kaons were produced by 400 GeV/c protons from the Fermilab main ring striking a 33 cm long beryllium oxide target. These were then sign- and momentum-selected (mean momentum, $\langle p \rangle$ ranging from 120 to 250 GeV/c for each polarity with $\Delta p/\langle p \rangle \approx 0.1$) by a set of magnets and beam collimators, collectively referred to as the dichromatic train. A fraction of these mesons subsequently decayed in a 350 m long evacuated region producing a beam of neutrinos and muons. Figure 2 shows, for a positive 250 GeV/c setting of the train, the reconstructed neutrino energy vs. the event radius at the detector. The upper band is due to neutrinos originating from two body kaon decays and the lower band from pion decays. The characteristic energy-radius correlation

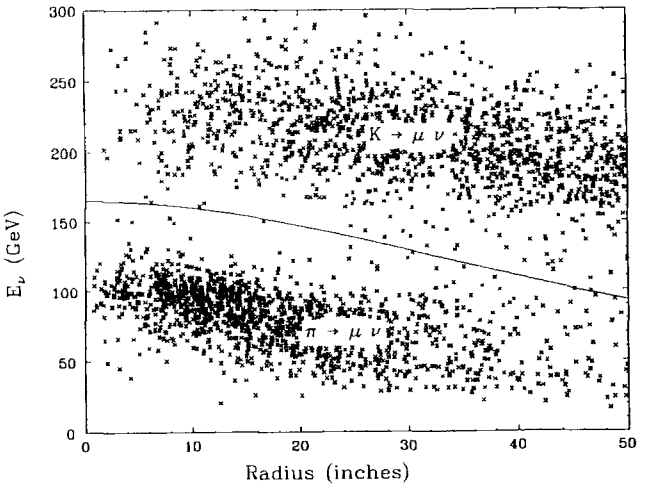

Fig. 2. Correlation of measured event energy, $E_\nu = E_\mu + E_{\text{had}}$, versus event radius at the Lab E detector for a 250 GeV/c setting of the secondary beam. The solid line is the energy separatrix between events induced by neutrinos from kaon decay and those from pion decay

originates from the boost of the isotropic two-body decay products of pions and kaons (in their rest frames) into the laboratory frame.

Two secondary beam monitoring stations [3] were located at 132 m and 310 m from the beginning of the decay region. The instrumentation relevant to this analysis include: a set of split plate ionization chambers used for steering the beam on a pulse by pulse basis; a set of segmented wire ionization chambers for measuring the beam's angular divergence; and a focusing Čerenkov counter for measuring particle fractions, the mean momentum and rms spread in momentum of the secondary beam. In this analysis, the Čerenkov counter was used only for momentum measurements: parent meson type (equivalent to particle fraction) was determined on an event by event basis from the measured energy-radius correlation.

Five different momentum settings of the train for both secondary polarities were selected during the two running periods. Nominal settings of ± 250, ± 200, ± 165, ± 140, and ± 120 GeV/c were used in E616 and $+250$, $+200$, ± 165, $+140$ and $+100$ GeV/c in E701.

The neutrino detector (Fig. 3) was located 940 m downstream of the secondary beam dump. The intervening earth and steel served as a muon filter. The detector was comprised of a target calorimeter with liquid scintillator counters and spark chambers followed by an iron toroidal muon spectrometer. The 690 ton iron target calorimeter consisted of six carts - each cart contained 14 scintillation counters (one each 10 cm of iron) and seven spark chambers (one each 20 cm of iron). The transverse size of the target was a 3 m square. The 310 ton muon spectrometer (17 kG) was also instrumented with scintillator counters and spark chambers. It consisted of three 3 m long iron toroidal magnets (containing 1.6 m of steel each) with a 1.8 m outer radius and a 12.7 cm radius hole for the coils. The target fiducial region consists of 280 tons for E616 and 160 tons for E701, or in

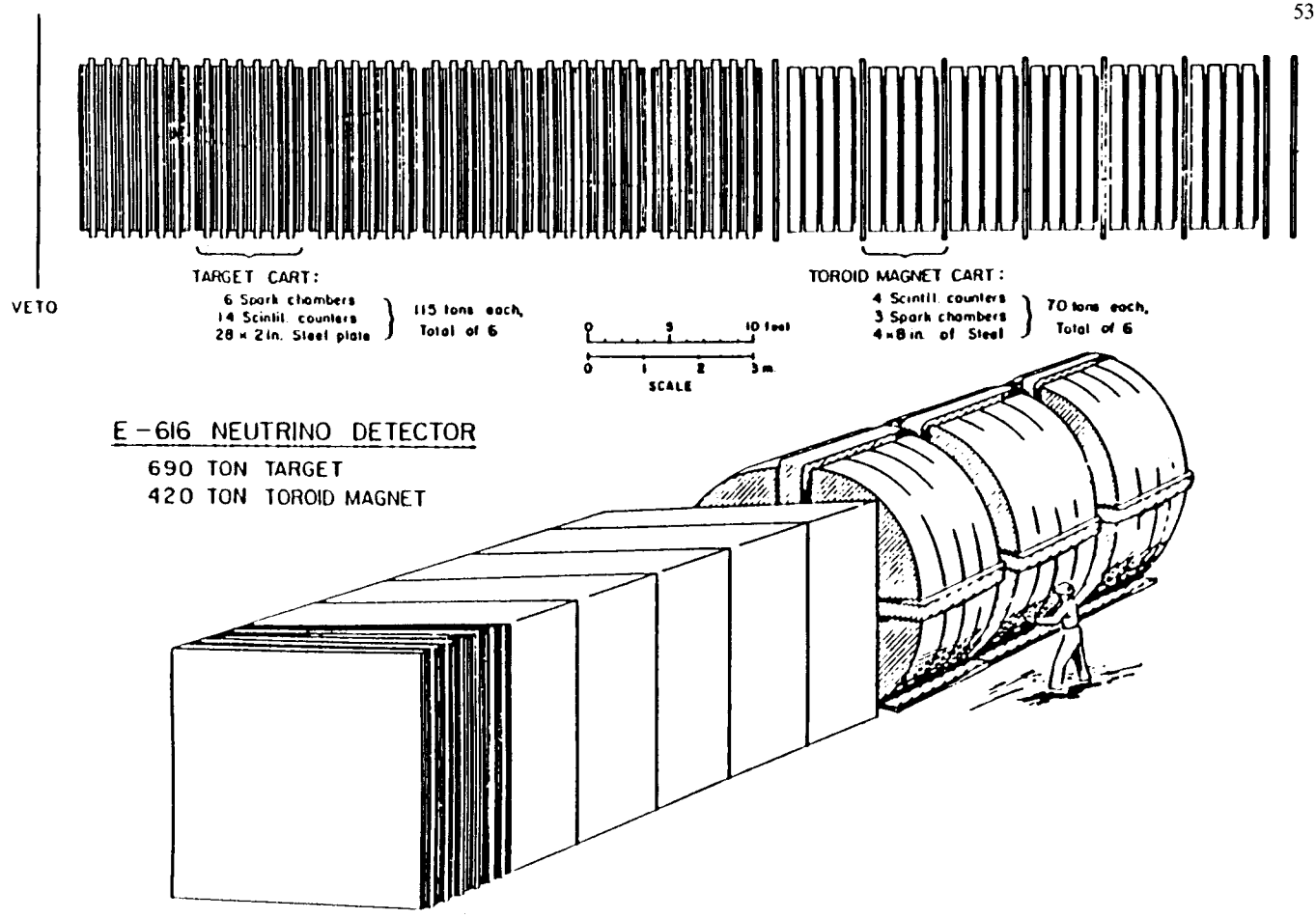

Fig. 3. Side view and perspective view of the Lab E detector

terms of density, 5360 gm/cm^2 and 3090 gm/cm^2 respectively.

The muon momentum resolution was limited by multiple scattering to $\delta|\mathbf{p}|/|\mathbf{p}| \simeq 11\%$. The muon angle resolution was also multiple-scattering limited and depended on how close to the primary vertex tracking could be achieved. The resolution on angle (θ_μ) may be parametrized as

$$\sigma_{\theta_\mu} = a + \frac{b}{|\mathbf{p}|}, \tag{5}$$

where a and b depend on hadron energy (E_{had}). The parameter a was always less then 0.26 mrad and b ranged from 80 to 156 (GeV/c) mrad as E_{had} varied from 10 to 300 GeV. The hadron energy calibration and resolution were determined using a beam of momentum analysed hadrons and muons in the range 25 to 250 GeV/c. The measured hadron energy resolution for charged current events was parametrized as

$$\sigma_{E_{\text{had}}} = (0.72 \pm 0.20) + (0.81 \pm 0.03)\sqrt{E_{\text{had}}} \tag{6}$$

where the energies are in GeV.

3 Structure function extraction

Structure functions were extracted from combinations of flux averaged neutrino and antineutrino differential cross sections evaluated at each (x, Q^2) bin center, formally defined as

$$\left\langle \frac{\mathrm{d}^2\sigma^{\nu(\bar{\nu})}}{\mathrm{d}x\,\mathrm{d}\log Q^2} \right\rangle_{\nu(\bar{\nu})} (x_0, Q_0^2) \equiv \frac{1}{\int \mathrm{d}E \Phi^{\nu(\bar{\nu})}(E)} \times \int \mathrm{d}E \Phi^{\nu(\bar{\nu})}(E) \frac{\mathrm{d}^2\sigma^{\nu(\bar{\nu})}}{\mathrm{d}x\,\mathrm{d}\log Q^2}(E, x_0, Q_0^2) \tag{7}$$

where $\Phi^{\nu(\bar{\nu})}$ is the number of neutrinos (antineutrinos) per GeV illuminating the Lab E detector. In terms of the measured differential cross sections, the structure functions in each (x, Q^2) bin were obtained from the following set of equations:

$$\left\langle \frac{\mathrm{d}^2\sigma^{\nu}}{\mathrm{d}x\,\mathrm{d}\log Q^2} \right\rangle_{\nu}^{\text{meas}} = \frac{G_F^2 M \ln 10}{\pi} [\langle a_2 \rangle_\nu F_2 + \langle a_3 \rangle_\nu x F_3 + \langle \delta^\nu \rangle_\nu] \tag{8}$$

$$\left\langle \frac{\mathrm{d}^2\sigma^{\bar{\nu}}}{\mathrm{d}x\,\mathrm{d}\log Q^2} \right\rangle_{\bar{\nu}}^{\text{meas}} = \frac{G_F^2 M \ln 10}{\pi} [\langle a_2 \rangle_{\bar{\nu}} F_2 - \langle a_3 \rangle_{\bar{\nu}} x F_3 + \langle \delta^{\bar{\nu}} \rangle_{\bar{\nu}}] \tag{9}$$

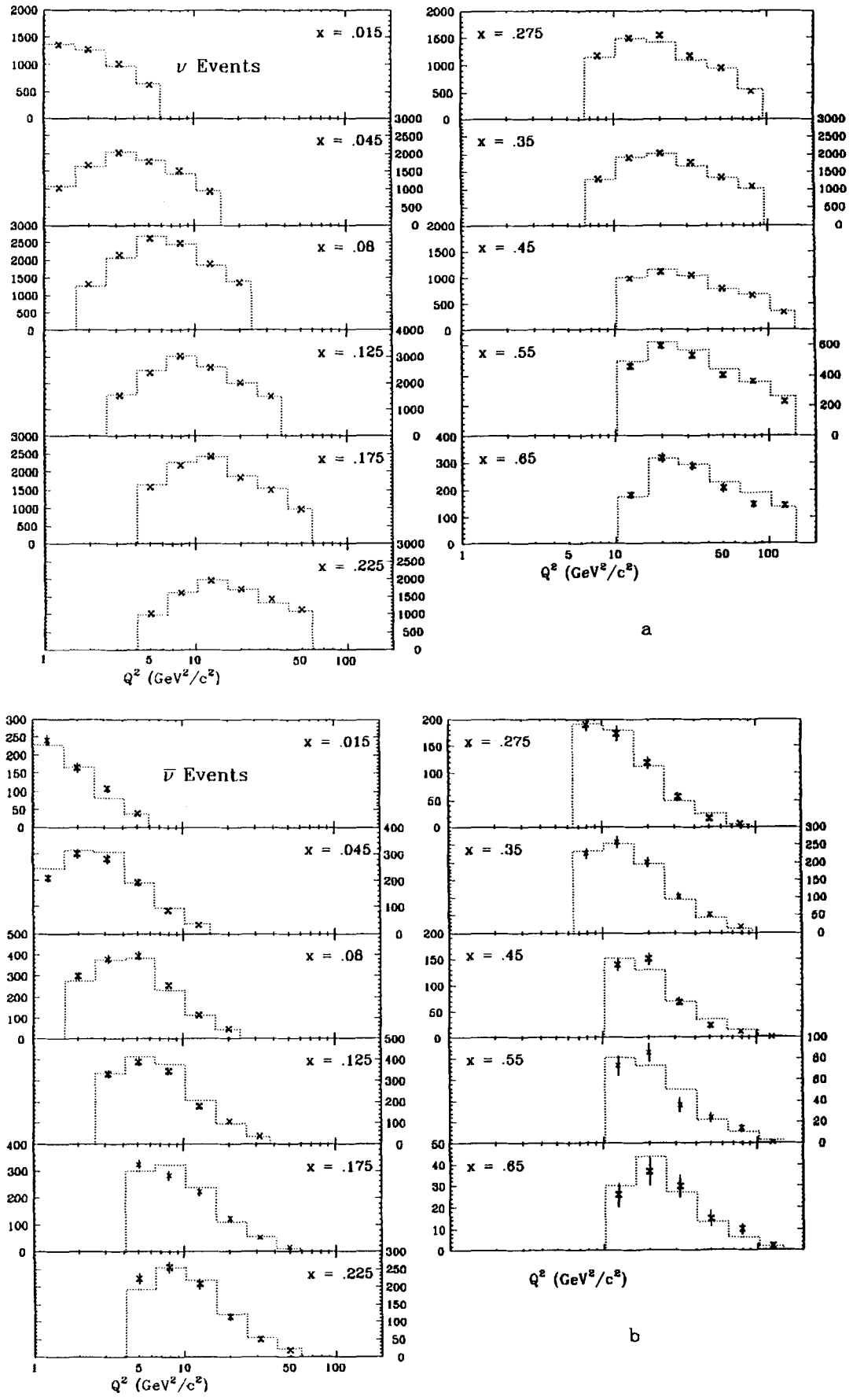

Fig. 4a, b. Comparisons of measured (crosses) and simulated (histograms) event sums in x and $\log Q^2$ bins for **a** neutrino induced and **b** antineutrino induced events

where

$$a_2 = Ey\left(1-y-\frac{Mxy}{2E}+\frac{y^2}{2}\,\frac{1+4M^2x^2/Q^2}{1+R(x,Q^2)}\right)$$

and

$$a_3 = Ey^2\left(1-\frac{y}{2}\right). \tag{10}$$

The $\delta^{\nu(\bar{\nu})}$ contain corrections due to isoscalar, strange sea and charm production threshold. Radiative effects [4] and propagator effects ($G_F \to G_F/(1+Q^2/M_W^2)$) were treated as multiplicative corrections to the differential cross sections (see below). These corrections are discussed in Appendix A.

The flux averaged differential cross sections in a given kinematic bin are proportional to the ratio of the measured event sum, N_{obs}, divided by the neutrino or antineutrino flux illuminating that bin. Resolution smearing, reconstruction efficiency, geometric acceptance and bin center corrections were calculated using a Monte Carlo simulation of the experiment. This simulation required (i) a parametrization of the energy and radial dependence of the neutrino and antineutrino flux spectra; (ii) a model of the detector resolution, reconstruction efficiency and acceptance; and (iii) a differential cross section model. The corrected, flux averaged differential cross sections, evaluated at the geometric center, assumed the form:

$$\left\langle \frac{\mathrm{d}^2\sigma^{\nu(\bar{\nu})}}{\mathrm{d}x\,\mathrm{d}\log Q^2}\right\rangle^{\mathrm{meas}}_{\nu(\bar{\nu})}(x_0,Q_0^2) = \frac{N^{\nu(\bar{\nu})}_{\mathrm{obs}}}{N^{\nu(\bar{\nu})}_{\mathrm{pred}}}\left\langle \frac{\mathrm{d}^2\sigma_0^{\nu(\bar{\nu})}}{\mathrm{d}x\,\mathrm{d}\log Q^2}\right\rangle_{\nu(\bar{\nu})}(x_0,Q_0^2), \tag{11}$$

where N_{pred} is the Monte Carlo event sum in that bin, generated with a physical ν-Fe cross section model and flux spectra, as well as detector resolution and acceptance. The model cross sections appearing here, $\sigma_0^{\nu(\bar{\nu})}$, differ from those used to calculate N_{pred}: in that the latter do not include radiative and propagator effects, whereas the former do. This procedure appropriately corrects for radiative and propagator effects.

The differential cross section model used in this procedure was constructed from fits to the extracted structure functions, iterating as required. Figure 4 shows the comparison between N_{pred} and N_{obs} as a function of x_0 and Q_0^2 for the final iteration.

3.1 Event analysis

Approximately 250 000 neutrino and 30 000 antineutrino induced charged current events were collected during the two running periods. Two types of triggers were used to obtain events for this analysis. Apart from the common veto counter requirement to remove events with charged particles at the front of the target, the two triggers were independent. The first type, the muon trigger, required only that a final state muon pass through the furthest downstream target cart and the first toroid of the spectrometer. The second type, the penetration trigger, required a 4 GeV energy deposition in the calorimeter and an event penetration length of at least 160 cm in the steel. Most events used in the structure function measurement satisfied the muon trigger requirements. Also included were those few events (1.8% for neutrinos and 1.3% for antineutrinos) with a low energy muon which pointed towards the spectrometer but stopped in the target. For these events, muon energy was determined from range.

Fiducial cuts applied to the event vertex position insured longitudinal and transverse containment of the hadronic shower. Additional cuts were applied to insure reliable neutrino flux modeling: events originating from pion and kaon decays were restricted to lie within a beam centered circular region of 76.2 cm and 127 cm radius respectively. (Cuts applied to the measured positions of the secondary beam on a spill by spill basis [3] maintained the projected neutrino beam center to within 3 cm at Lab *E*.) Good geometric acceptance was maintained by including only those events with the final state muon angle $\theta_\mu < 200$ mrad. Cuts on the projected positions of the muon at the spectrometer insured a high likelihood ($> 96\%$) for momentum reconstruction. Most events failing reconstruction cuts were treated interactively, reconstructed, and then used to parametrize the reconstruction inefficiency as a function of muon momentum.

A minimum muon energy of 4 GeV at the event vertex was required to insure penetration beyond the hadron shower end. A cut on hadron energies below 10 GeV eliminated the region of poor x-resolution at low values of Q^2. An additional cut on events with $Q^2 < 1$ $(\mathrm{GeV/c})^2$ eliminated a small region at low values of x where the Q^2 resolution is poor. The final event sample after all cuts consisted of 88 491 neutrino and 9 252 antineutrino induced events.

3.2 Flux analysis

Traditionally, calculation of the dichromatic flux spectrum had been based entirely on the measured properties of the secondary beam [3]: (a) The energy and radial dependence of the flux was computed from the measured momentum spectrum (mean and rms spread) and angular divergence of the secondary beam and (b) the normalizations were computed from the measured intensities and particle fractions. In this analysis, only the secondary beam measurements pertaining to (a) were used. The ability to separate pion-induced from kaon-induced events, together with consistency requirements applied to the measured event distributions, were used to establish relative neutrino flux normalizations.

At each setting, i, of the secondary beam the neutrino flux $\phi_i(E,r)$ = number of ν's/GeV/cm^2 at the Lab E detector, was expressed as:

$$\phi_i(E,r) = \mathrm{N}^i_\pi \phi^\pi_i(E,r) + N^i_K \phi^K_i(E,r) + \phi^{WB}_i(E,r), \tag{12}$$

where N_π and N_K are the pion and kanon intensities. The flux appearing in (7) is given by $\Phi(E) = \int_0^{r_{max}} dr\phi(E,r)$, where $r_{max} = 76.4$ cm or 127 cm for E_ν less than or greater than the energy separatrix, $E^{SEP}(r)$ (shown as a solid line for a 250 GeV/c setting in Fig. 1). ϕ^π and ϕ^K are the neutrino flux at Lab E per pion or kaon respectively and ϕ^{WB} is the wideband neutrino flux originating from secondary decays prior to momentum selection.

The calculation of ϕ_i^π and ϕ_i^K, detailed in [3, 5], is outlined here. Pion and kaon rays were first generated by using measured secondary production spectra from p-BeO as input to a ray tracing model of the dichromatic train. Small adjustments to these rays were then made to match the measured secondary profiles, $\langle p \rangle$ and σ_p. ϕ_i^π and ϕ_i^K were then obtained from a simulation of their decays in accordance with the known branching ratios and kinematic constraints.

Determination of the flux normalization was divided into two steps: first, the relative flux contributions from both parent types and all settings of a given polarity were determined. Only after these relative normalizations were specified could the data from different energy settings be combined. The second step involved determining the absolute flux levels for neutrinos and antineutrinos. This latter procedure is discussed in Appendix B.

The relative normalizations N_i^π and N_i^K (12), with i ranging over all positive settings, were determined by requiring that the simulated event sums (passing the structure function cuts) from the corresponding settings and parent types were in the same proportions as the measured event sums*. The relative normalizations for i, ranging over negative settings, were determined separately using an identical procedure.

The ϕ_i^{WB}, appearing in (12), was measured by scaling the number of events measured during special runs taken with the momentum defining collimator (in the secondary beamline) closed by the ratio of the total protons on target during normal runs to the total protons on target during collimator closed runs. The energy dependence of ϕ_i^{WB} was fit to an empirical functional form [6], and used to simulate wideband event contamination. Measured event sums in each (x, $\log Q^2$) bin obtained during normal (open collimator) runs were then corrected for the wideband contamination by subtracting the simulated event sums.

Figure 5a shows the neutrino flux spectra for a 250 GeV/c setting for beam centered radius $r < 10$ inches, showing the clear separation of pions due to pion and kaon decays. Also shown are the flux of neutrinos from $K_{\mu 3}$ decays and wideband decays. Figure 5b shows the flux from the same setting integrated over the entire fiducial region. The kinks in the wideband and $K_{\mu 3}$ decay spectra are due to energy dependent radial cuts. Figure 6 shows the cumulative neutrino and antineutrino flux spectra.

* This procedure is valid so long as the structure functions used in the simulation do not depend on the neutrino energy and that the energy dependence of the cross sections is given by (8) and (9)

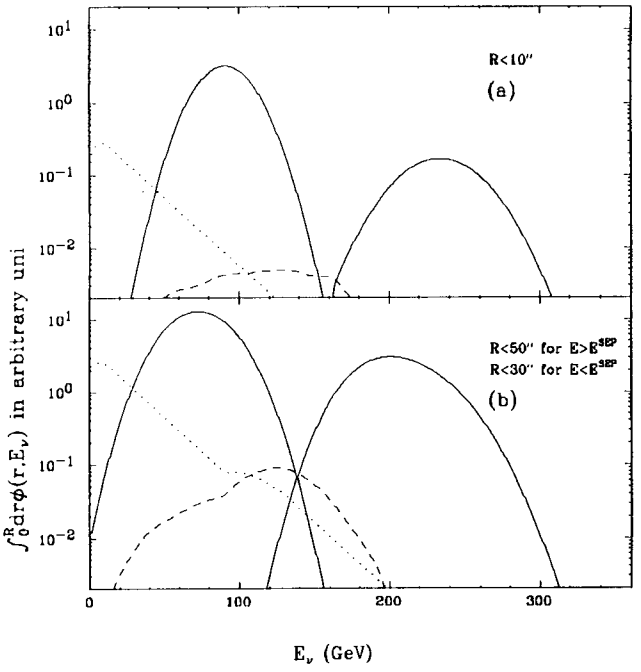

Fig. 5a, b. Energy spectrum of the neutrino flux for a +250 GeV/c setting of the secondary hadron beam at the Lab E detector for **a** radius less than 10 inches and **b** the full fiducial region. The solid curves represent the neutrino flux orginating from two-body pion (low energy) and kaon (high energy) decays, the dashed lines are from neutrinos originating from $K \to \pi^0 \mu \nu$ decays and the dotted lines are from neutrinos originating from secondary decays prior to momentum selection (wide band decays)

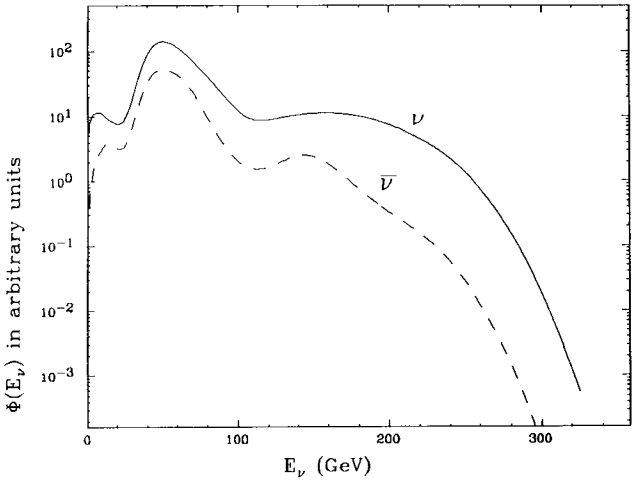

Fig. 6. Cumulative neutrino (solid line) and antineutrino (dashed line) energy spectra at the Lab E detector, integrated over the full fiducial region for all settings of the secondary beam

3.3 Results

Table 1 lists the extracted structure functions along with statistical errors. Included in the Table are the statistical correlations, $\Delta_{F_2}\Delta_{xF_3}$. Figure 7 shows the extracted structure functions with statistical errors. Table 2 lists F_2 and

Table 1. Structure function results with statistical errors. The last column is the correlation between F_2 and xF_3

x	Q^2	F_2	ΔF_2	xF_3	ΔxF_3	$\Delta F_2 \Delta xF_3$
0.015	1.26	1.2278	0.0358	0.2607	0.0456	-0.5466E-03
	2.00	1.2571	0.0434	0.3062	0.0564	-0.1134E-02
	3.16	1.5166	0.0615	0.2361	0.0681	-0.2383E-02
	5.01	1.4460	0.0985	0.2954	0.0865	-0.5829E-02
0.045	1.26	1.1808	0.0405	0.6817	0.1469	-0.2212E-02
	2.00	1.3722	0.0360	0.6191	0.0792	-0.8951E-03
	3.16	1.3618	0.0347	0.5812	0.0501	-0.4171E-03
	5.01	1.4457	0.0422	0.5493	0.0554	-0.7553E-03
	7.94	1.6003	0.0620	0.7399	0.0797	-0.2719E-02
	12.59	1.5402	0.0928	0.6497	0.0902	-0.5191E-02
0.080	2.00	1.3805	0.0386	0.7043	0.1589	-0.2132E-02
	3.16	1.4177	0.0327	0.7671	0.0818	-0.7809E-03
	5.01	1.4244	0.0305	0.6416	0.0483	-0.2532E-03
	7.94	1.5256	0.0351	0.7038	0.0447	-0.2597E-03
	12.59	1.5654	0.0512	0.7736	0.0700	-0.1686E-02
	19.95	1.5362	0.0690	0.7226	0.0721	-0.2592E-02
0.125	3.16	1.2806	0.0344	0.6479	0.1397	-0.1611E-02
	5.01	1.2774	0.0289	0.8022	0.0712	-0.4858E-03
	7.94	1.3363	0.0271	0.8675	0.0424	-0.8042E-04
	12.59	1.3185	0.0315	0.8833	0.0412	-0.9021E-04
	19.95	1.4574	0.0453	0.7477	0.0626	-0.1211E-02
	31.62	1.3788	0.0564	0.8543	0.0596	-0.1323E-02
0.175	5.01	1.1841	0.0313	0.6474	0.1111	-0.9716E-03
	7.94	1.1059	0.0269	0.8935	0.0583	-0.1897E-03
	12.59	1.1721	0.0268	0.8743	0.0402	0.4931E-04
	19.95	1.1914	0.0333	0.7912	0.0469	-0.1361E-03
	31.62	1.1407	0.0426	0.7872	0.0561	-0.7424E-03
	50.12	1.1604	0.0590	0.8152	0.0607	-0.1128E-02
0.225	5.01	1.1012	0.0353	0.5914	0.1642	-0.1876E-02
	7.94	1.0420	0.0280	0.8203	0.0792	-0.4218E-03
	12.59	1.0172	0.0253	0.8276	0.0454	0.2606E-04
	19.95	0.9968	0.0275	0.8127	0.0392	0.1442E-03
	31.62	1.0525	0.0368	0.9035	0.0548	-0.4533E-03
	50.12	0.9719	0.0401	0.7945	0.0463	-0.1961E-03
x	Q^2	F_2	ΔF_2	xF_3	ΔxF_3	$\Delta F_2 \Delta xF_3$
0.275	7.94	0.8922	0.0282	0.8220	0.0994	-0.6422E-03
	12.59	0.8530	0.0245	0.7666	0.0534	-0.5666E-04
	19.95	0.9060	0.0246	0.7839	0.0377	0.1686E-03
	31.62	0.8810	0.0303	0.7432	0.0458	-0.2921E-04
	50.12	0.7723	0.0346	0.7593	0.0459	-0.1270E-03
	79.43	0.7853	0.0480	0.6137	0.0510	-0.1599E-03
0.350	7.94	0.6887	0.0209	0.6838	0.0956	-0.5649E-03
	12.59	0.6593	0.0167	0.6378	0.0466	-0.9393E-04
	19.95	0.6415	0.0155	0.5701	0.0283	0.5179E-04
	31.62	0.6519	0.0171	0.5860	0.0268	0.6781E-04
	50.12	0.6019	0.0212	0.5045	0.0330	-0.9902E-04
	79.43	0.6018	0.0219	0.5320	0.0256	0.1100E-03
0.450	12.59	0.4308	0.0157	0.4721	0.0574	-0.1956E-03
	19.95	0.4206	0.0136	0.3237	0.0314	-0.7874E-05
	31.62	0.3942	0.0135	0.3949	0.0228	0.6567E-04
	50.12	0.3488	0.0160	0.4001	0.0268	0.1210E-05
	79.43	0.3319	0.0166	0.3501	0.0230	0.3695E-04
	125.89	0.2884	0.0210	0.2970	0.0233	0.1703E-03
0.550	12.59	0.2571	0.0140	0.2836	0.0632	-0.2454E-03
	19.95	0.2515	0.0112	0.2162	0.0314	-0.3591E-04
	31.62	0.2058	0.0107	0.2296	0.0210	0.1963E-04
	50.12	0.1893	0.0114	0.1746	0.0201	0.1576E-04
	79.43	0.2015	0.0132	0.1637	0.0216	-0.4163E-04
	125.89	0.1414	0.0131	0.1516	0.0157	0.6088E-04
0.650	12.59	0.1446	0.0127	0.2040	0.0690	-0.3041E-03
	19.95	0.1213	0.0081	0.1384	0.0272	-0.4921E-04
	31.62	0.1164	0.0075	0.1081	0.0167	0.1951E-06
	50.12	0.0920	0.0077	0.0719	0.0143	-0.1149E-05
	79.43	0.0824	0.0086	0.0464	0.0155	-0.2547E-04
	125.89	0.0758	0.0084	0.0725	0.0112	0.3548E-05

xF_3 along with estimates of the important systematic errors. The first four columns are the estimated changes in the structure function due to changes, of about 1%, in the various energy scale(s). The last two columns show the changes resulting from a 10% increase in the assumed angular divergence of the secondary beam and 1.7% increase in the relative antineutrino to neutrino flux level (keeping the sum of neutrino and antineutrino total cross section slopes unchanged). The correlated neutrino/antineutrino flux uncertainty of 3.1% translates directly to an overall uncertainty of both F_2 and xF_3. The overall error on an individual value of F_2 and xF_3 is evaluated by evaluating the quadratic sum of the various terms of Table 2 and the 3.1% overall normalization error above. The errors due to these systematic effects are, however, correlated. Hence, in general, the procedure for utilizing the full table is more complicated (see Sect. 4.4 Scaling violation under Sect. 4.4.1 Fitting procedure).

4 Discussion of results

Our structure function results are compared with those from other deep inelastic scattering experiments and theoretical models. Direct comparisons among different structure function results are complicated by the differences in assumptions (total cross section slopes and model corrections) used in each analysis. For all comparisons discussed here, structure functions from the present data set were extracted with the assumptions used in the other analyses. Tests of the quark parton model (QPM) include direct comparison with results from charged lepton scattering experiments, in order to measure the mean squared charge of quarks in the nucleon, and the Gross-Llewellyn Smith (GLS) sum rule [7] which measures the valence quark content of the nucleon. Scaling violations are analysed in the context of perturbative QCD. The Altarelli-Parisi evolution equations [8] were used to determine the QCD scale parameter, Λ, and to determine, to the extent possible, the shape of the unmeasured gluon momentum density.

4.1 Comparisons with other neutrino results

The present data sample is about 1.5 times larger then that published by this group in 1984. In addition to an increase in statistics, the changes in the analysis methods and assumptions have resulted in small differences between the results presented here and those previously published (1984) by this group [9]. The present analysis relied on the y-intercept method (see Appendix B) to constrain the neutrino to antineutrino cross section: In the process, $\sigma^{\bar{\nu}}/\sigma^{\nu}$ decreased from 0.508 to 0.492, a change consistent with the quoted 3.5% uncorrelated flux uncertainty. An improvement made in the parametrization of the QCD predicted value of $R=\sigma_L/\sigma_T$ affected F_2, primarily at small values x. In addition, other improvements in the analysis method, primarily in the treatment of resolution smearing, resulted in small additional changes in the x-dependence of the structure functions

Table 2 (a)

x	Q^2	F_2	Stat.	E_{had}	E_μ	E	p_{secy}	$\Delta_{\theta_{sec}}$	$\Phi^{\bar{\nu}}/\Phi^{\nu}$
0.015	1.26	1.2278	0.0358	0.0013	-.0157	-.0171	-.0015	0.0015	-.0006
	2.00	1.2571	0.0434	0.0084	-.0196	-.0198	-.0096	0.0005	-.0007
	3.16	1.5166	0.0615	0.0244	-.0169	-.0134	-.0193	0.0011	-.0007
	5.01	1.4460	0.0985	0.0179	-.0286	-.0373	-.0259	0.0002	-.0008
0.045	1.26	1.1808	0.0405	-.0102	-.0192	-.0191	0.0073	-.0012	-.0015
	2.00	1.3722	0.0360	-.0086	-.0192	-.0194	0.0053	-.0005	-.0009
	3.16	1.3618	0.0347	0.0029	-.0169	-.0185	-.0023	0.0025	0.0002
	5.01	1.4457	0.0422	0.0128	-.0185	-.0166	-.0135	0.0006	0.0007
	7.94	1.6003	0.0620	0.0162	-.0193	-.0235	-.0174	-.0006	0.0003
	12.59	1.5402	0.0928	0.0341	-.0186	-.0110	-.0325	0.0059	0.0011
0.080	2.00	1.3805	0.0386	-.0105	-.0177	-.0247	0.0087	-.0023	-.0017
	3.16	1.4177	0.0327	-.0042	-.0176	-.0163	0.0075	0.0015	-.0007
	5.01	1.4244	0.0305	-.0039	-.0218	-.0220	-.0010	0.0036	0.0007
	7.94	1.5256	0.0351	0.0201	-.0134	-.0131	-.0144	0.0010	0.0018
	12.59	1.5654	0.0512	0.0145	-.0162	-.0094	-.0158	0.0003	0.0011
	19.95	1.5362	0.0690	0.0287	-.0136	-.0174	-.0286	0.0055	0.0023
0.125	3.16	1.2806	0.0344	-.0141	-.0124	-.0146	0.0098	-.0009	-.0012
	5.01	1.2774	0.0289	-.0085	-.0138	-.0154	0.0055	0.0017	-.0002
	7.94	1.3363	0.0271	0.0025	-.0121	-.0121	-.0031	0.0044	0.0014
	12.59	1.3185	0.0315	0.0135	-.0071	-.0089	-.0142	0.0023	0.0024
	19.95	1.4574	0.0453	0.0107	-.0161	-.0124	-.0139	-.0017	0.0020
	31.62	1.3788	0.0564	0.0293	-.0046	-.0053	-.0248	0.0079	0.0033
0.175	5.01	1.1841	0.0313	-.0075	-.0103	-.0109	0.0071	0.0009	-.0006
	7.94	1.1059	0.0269	-.0019	-.0034	-.0044	0.0033	0.0028	0.0006
	12.59	1.1721	0.0268	0.0067	-.0071	-.0079	-.0071	0.0037	0.0021
	19.95	1.1914	0.0333	0.0139	-.0055	-.0059	-.0131	0.0000	0.0025
	31.62	1.1407	0.0426	0.0079	-.0084	-.0096	-.0109	0.0017	0.0025
	50.12	1.1604	0.0590	0.0296	-.0003	-.0033	-.0316	0.0079	0.0037
0.225	5.01	1.1012	0.0353	-.0146	-.0076	-.0100	0.0073	0.0000	-.0009
	7.94	1.0420	0.0280	-.0058	-.0050	-.0032	0.0051	0.0021	0.0002
	12.59	1.0172	0.0253	0.0006	-.0012	-.0024	-.0003	0.0046	0.0015
	19.95	0.9968	0.0275	0.0081	0.0005	-.0014	-.0110	0.0014	0.0025
	31.62	1.0525	0.0368	0.0065	0.0019	-.0048	-.0089	0.0000	0.0023
	50.12	0.9719	0.0401	0.0137	-.0017	-.0012	-.0137	0.0033	0.0033
0.275	7.94	0.8922	0.0282	-.0039	0.0051	0.0024	0.0048	0.0010	-.0001
	12.59	0.8530	0.0245	-.0018	0.0034	0.0031	0.0003	0.0030	0.0010
	19.95	0.9060	0.0246	0.0060	0.0050	-.0028	-.0075	0.0020	0.0022
	31.62	0.8810	0.0303	0.0056	-.0038	0.0008	-.0098	0.0000	0.0023
	50.12	0.7723	0.0346	0.0051	0.0034	-.0021	-.0085	0.0017	0.0024
	79.43	0.7853	0.0480	0.0292	0.0075	0.0063	-.0247	0.0061	0.0033
0.350	7.94	0.6887	0.0209	-.0068	0.0074	0.0024	0.0041	0.0008	-.0003
	12.59	0.6593	0.0167	-.0057	0.0014	0.0004	0.0017	0.0021	0.0004
	19.95	0.6415	0.0155	-.0008	0.0066	0.0028	-.0034	0.0023	0.0013
	31.62	0.6519	0.0171	0.0039	0.0108	0.0078	-.0070	0.0007	0.0019
	50.12	0.6019	0.0212	0.0013	0.0043	0.0021	-.0055	0.0006	0.0016
	79.43	0.6018	0.0219	0.0086	0.0076	0.0053	-.0110	0.0032	0.0025
0.450	12.59	0.4308	0.0157	-.0023	0.0109	0.0071	0.0014	0.0013	0.0000
	19.95	0.4206	0.0136	-.0034	0.0082	0.0047	-.0013	0.0010	0.0006
	31.62	0.3942	0.0135	-.0013	0.0088	0.0055	-.0039	0.0004	0.0011
	50.12	0.3488	0.0160	0.0001	0.0091	0.0038	-.0040	-.0002	0.0010
	79.43	0.3319	0.0166	-.0004	0.0053	0.0019	-.0039	0.0010	0.0012
	125.89	0.2884	0.0210	0.0106	0.0094	0.0087	-.0089	0.0023	0.0014
0.550	12.59	0.2571	0.0140	-.0054	0.0071	0.0056	0.0011	0.0007	-.0001
	19.95	0.2515	0.0112	-.0009	0.0083	0.0056	-.0005	0.0009	0.0002
	31.62	0.2058	0.0107	-.0008	0.0064	0.0032	-.0018	0.0008	0.0004
	50.12	0.1893	0.0114	-.0004	0.0088	0.0049	-.0026	0.0001	0.0005
	79.43	0.2015	0.0132	-.0004	0.0113	0.0080	-.0016	0.0003	0.0006
	125.89	0.1414	0.0131	0.0027	0.0048	0.0041	-.0031	0.0009	0.0006
0.650	12.59	0.1446	0.0127	-.0024	0.0017	-.0012	0.0001	0.0005	-.0001
	19.95	0.1213	0.0081	-.0023	0.0067	0.0047	-.0002	0.0006	0.0000
	31.62	0.1164	0.0075	-.0009	0.0066	0.0044	-.0008	0.0004	0.0002
	50.12	0.0920	0.0077	-.0013	0.0053	0.0042	-.0012	0.0001	0.0002
	79.43	0.0824	0.0086	-.0009	0.0033	0.0020	-.0011	0.0001	0.0002
	125.89	0.0758	0.0084	-.0008	0.0059	0.0049	-.0010	0.0006	0.0003

Table 2a, b. Structure function results with systematic errors for **a** F_2 and **b** xF_3. The columns labeled E_{had}, E_μ, E and $p_{\mathrm{sec}\,y}$ show the changes in the reported structure functions due to an increase of 1% in the hadron energy calibration, the muon momentum calibration, all energy calibrations and the secondary momentum calibration respectively. $\Delta\theta_{\mathrm{sec}}$ corresponds to the changes in structure functions for a 10% increase in the angular dispersion of the secondary beam. $\Phi^{\bar{\nu}}/\Phi^{\nu}$ corresponds to the changes in the structure functions for a 1.7% increase in the antineutrino-to-neutrino normalization

Table 2 (b)

x	Q^2	xF_3	Stat.	E_{had}	E_μ	E	p_{secy}	$\Delta_{\theta_{xz}}$	$\Phi^{\bar{\nu}}/\Phi^{\nu}$
0.015	1.26	0.2607	0.0456	-.0017	-.0042	-.0048	0.0018	0.0014	0.0106
	2.00	0.3062	0.0564	0.0001	-.0061	-.0046	0.0033	0.0027	0.0123
	3.16	0.2361	0.0681	-.0024	-.0045	-.0031	0.0012	0.0013	0.0081
	5.01	0.2954	0.0865	0.0000	-.0005	0.0018	0.0001	0.0021	0.0085
0.045	1.26	0.6817	0.1469	-.0144	-.0280	-.0213	0.0153	0.0121	0.0509
	2.00	0.6191	0.0792	-.0071	-.0186	-.0092	0.0129	0.0055	0.0266
	3.16	0.5812	0.0501	-.0047	-.0156	-.0141	0.0053	0.0034	0.0158
	5.01	0.5493	0.0554	0.0000	-.0171	-.0141	0.0039	0.0041	0.0134
	7.94	0.7399	0.0797	0.0043	-.0116	-.0048	0.0066	0.0046	0.0183
	12.59	0.6497	0.0902	0.0083	-.0073	-.0041	-.0034	0.0020	0.0124
0.080	2.00	0.7043	0.1589	-.0049	-.0049	0.0092	0.0159	0.0085	0.0450
	3.16	0.7671	0.0818	-.0115	-.0220	-.0310	0.0136	0.0018	0.0288
	5.01	0.6416	0.0483	-.0026	-.0070	-.0013	0.0059	0.0036	0.0147
	7.94	0.7039	0.0447	0.0023	-.0146	-.0100	0.0008	0.0030	0.0127
	12.59	0.7736	0.0700	-.0037	-.0162	-.0203	0.0016	0.0018	0.0155
	19.95	0.7226	0.0721	0.0016	-.0089	-.0106	-.0035	0.0044	0.0109
0.125	3.16	0.6479	0.1397	-.0053	-.0251	-.0145	0.0130	0.0049	0.0330
	5.01	0.8022	0.0712	-.0126	-.0286	-.0346	0.0122	0.0033	0.0240
	7.94	0.8675	0.0424	-.0026	-.0127	-.0069	0.0047	0.0058	0.0158
	12.59	0.8833	0.0412	0.0047	-.0107	-.0091	-.0012	0.0041	0.0130
	19.95	0.7477	0.0626	0.0026	-.0126	-.0162	-.0008	0.0013	0.0119
	31.62	0.8543	0.0596	0.0086	-.0048	-.0016	-.0043	0.0068	0.0101
0.175	5.01	0.6474	0.1111	-.0105	-.0010	-.0043	0.0104	0.0004	0.0244
	7.94	0.8936	0.0583	-.0020	-.0022	0.0025	0.0088	0.0030	0.0197
	12.59	0.8743	0.0402	-.0016	-.0091	-.0092	0.0008	0.0060	0.0128
	19.95	0.7912	0.0469	0.0053	-.0091	-.0059	-.0029	0.0013	0.0106
	31.62	0.7872	0.0561	-.0066	-.0132	-.0111	-.0006	0.0011	0.0098
	50.12	0.8152	0.0607	0.0198	-.0072	-.0056	-.0096	0.0069	0.0078
0.225	5.01	0.5914	0.1642	0.0115	-.0050	-.0042	0.0115	0.0056	0.0264
	7.94	0.8203	0.0792	-.0204	-.0108	0.0016	0.0124	0.0025	0.0216
	12.59	0.8276	0.0454	-.0014	-.0104	-.0107	0.0046	0.0045	0.0131
	19.95	0.8127	0.0392	-.0011	0.0010	-.0003	-.0030	0.0026	0.0097
	31.62	0.9035	0.0548	0.0088	-.0092	-.0098	-.0026	0.0007	0.0114
	50.12	0.7945	0.0463	0.0007	-.0049	-.0038	-.0043	0.0032	0.0074
0.275	7.94	0.8220	0.0994	-.0109	-.0149	-.0339	0.0112	0.0042	0.0250
	12.59	0.7666	0.0534	-.0107	-.0201	-.0091	0.0060	0.0037	0.0137
	19.95	0.7839	0.0377	0.0044	-.0028	-.0076	-.0021	0.0033	0.0094
	31.62	0.7432	0.0458	0.0001	0.0013	-.0009	-.0047	0.0012	0.0086
	50.12	0.7593	0.0459	-.0013	-.0010	-.0003	-.0002	0.0013	0.0075
	79.43	0.6137	0.0510	0.0152	0.0039	0.0001	-.0146	0.0047	0.0047
0.350	7.94	0.6838	0.0956	-.0135	0.0073	-.0131	0.0107	0.0024	0.0251
	12.59	0.6378	0.0466	-.0125	0.0045	0.0045	0.0070	0.0038	0.0138
	19.95	0.5701	0.0283	-.0034	0.0077	0.0042	0.0010	0.0027	0.0076
	31.62	0.5860	0.0268	0.0007	0.0018	0.0030	-.0032	0.0021	0.0064
	50.12	0.5045	0.0330	-.0021	0.0047	0.0020	0.0004	0.0011	0.0055
	79.43	0.5320	0.0256	0.0058	0.0086	0.0083	-.0056	0.0029	0.0041
0.450	12.59	0.4721	0.0574	-.0131	0.0121	0.0140	0.0080	0.0026	0.0130
	19.95	0.3237	0.0314	-.0053	0.0013	0.0000	0.0014	0.0023	0.0053
	31.62	0.3949	0.0228	-.0020	0.0081	0.0029	-.0019	0.0015	0.0045
	50.12	0.4001	0.0268	-.0004	0.0118	0.0082	-.0020	0.0003	0.0045
	79.43	0.3501	0.0230	-.0025	0.0049	-.0005	-.0018	0.0014	0.0031
	125.89	0.2970	0.0233	0.0093	0.0081	0.0075	-.0090	0.0022	0.0020
0.550	12.59	0.2836	0.0632	0.0031	0.0080	0.0041	0.0059	0.0018	0.0098
	19.95	0.2162	0.0314	-.0036	0.0078	0.0079	0.0011	0.0015	0.0044
	31.62	0.2296	0.0210	-.0016	0.0072	0.0051	0.0001	0.0014	0.0031
	50.12	0.1746	0.0201	0.0009	0.0085	0.0076	-.0008	0.0004	0.0020
	79.43	0.1637	0.0216	-.0035	0.0042	0.0015	-.0009	0.0002	0.0017
	125.89	0.1516	0.0157	0.0021	0.0057	0.0048	-.0024	0.0011	0.0011
0.650	12.59	0.2040	0.0690	-.0059	0.0055	0.0132	0.0015	-.0025	0.0084
	19.95	0.1385	0.0272	-.0037	0.0100	0.0009	0.0014	0.0014	0.0034
	31.62	0.1081	0.0167	-.0015	0.0053	0.0032	0.0000	0.0004	0.0017
	50.12	0.0719	0.0143	-.0015	0.0041	0.0029	-.0005	0.0004	0.0009
	79.43	0.0464	0.0155	-.0001	0.0023	0.0017	-.0004	0.0003	0.0005
	125.89	0.0725	0.0112	-.0015	0.0049	0.0028	-.0006	0.0008	0.0006

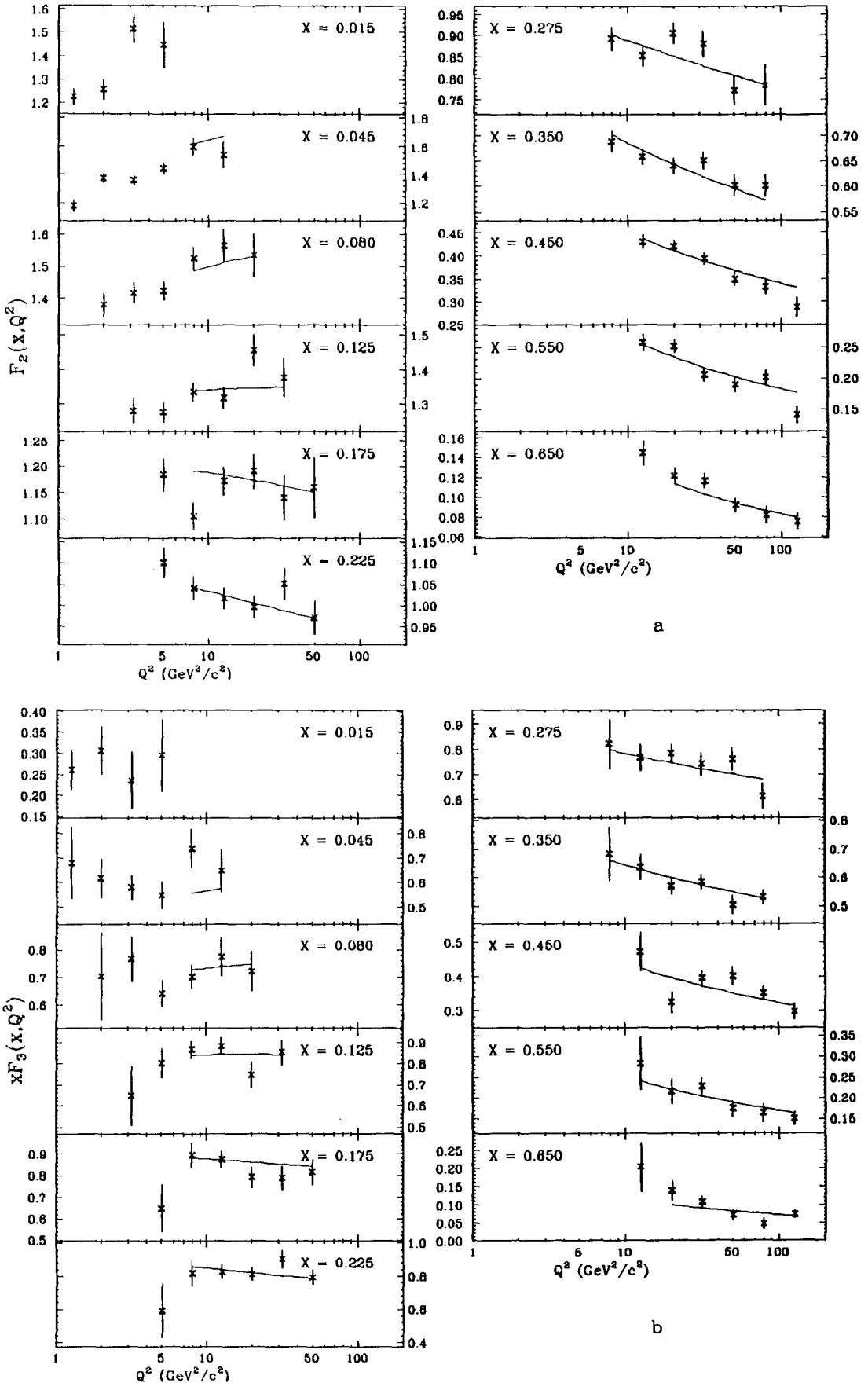

Fig. 7a, b. Extracted values of **a** F_2 and **b** xF_3. The solid curves are next to leading order fits to QCD, described in Sect. 4.3

from the 1984 results: the extracted values of F_2 and xF_3 are lower at small and large values of x and higher at intermediate value (see Fig. 8).

Table 3 shows the numbers of events, cross section slopes and some parameters relating to model assumptions entering into the structure function analysis for several recent experiments reporting isoscalar structure functions [9–12]. Figure 8 shows the ratio $F^{\mathrm{OTHER}}/F^{\mathrm{CCFR}}$ as a function of x, where F^{CCFR} has been extracted using the respective assumptions of the other analysis. For each plotted point, the ratio was formed by interpolating both data sets to the geometric mean value of the Q^2 range common to both experiments. Only statistical errors are shown.

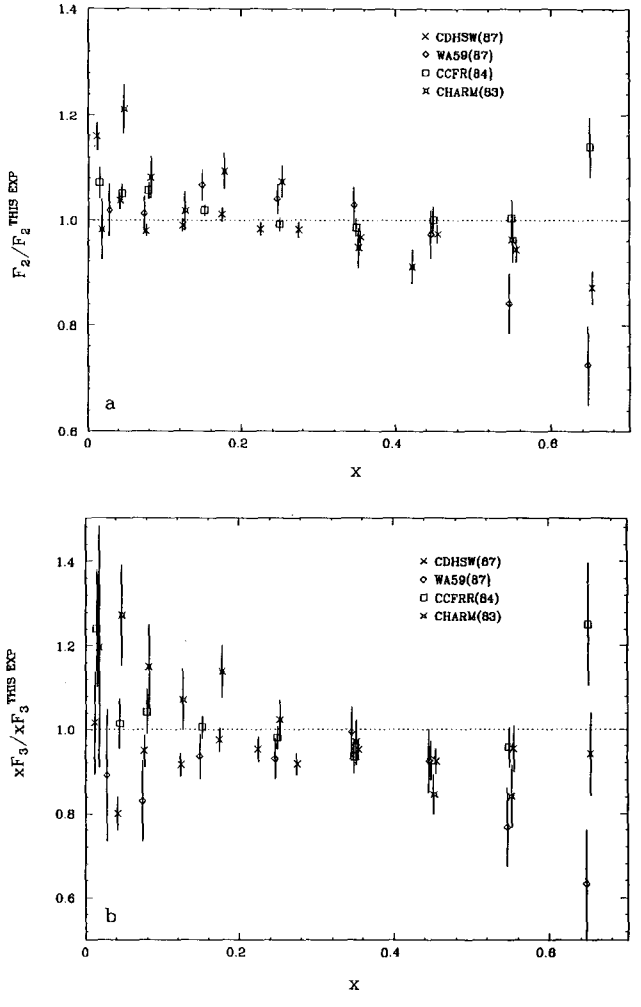

Fig. 8a, b. Ratio of $F^{\mathrm{OTHER}}/F^{\mathrm{CCFR}}$ as a function of x with the adjustment of the CCFR assumptions to match the other's: **a** F_2 and **b** xF_3

4.2 Mean squared charge test

Comparison of F_2 measurements from charged lepton and neutrino scattering experiments, test the value of the mean squared charge of the scattered nucleon constituents. While the strong interaction modifies many QPM predictions (e.g. scaling), these effects are expected to cancel in the ratio:

$$F_2^{l^{\pm}N} = \frac{5}{18}\left(1 - \frac{3}{5}\frac{s+\bar{s}}{q+\bar{q}}\right)\cdot F_2^{\nu N}, \tag{13}$$

where 5/18 is the mean squared charge of quarks in the nucleon and the small correction term accounts for the $s-c$ asymmetry (c is assumed zero). This comparison requires correction for the threshold behavior for the weak $d, s \to c$ transitions which are not present in electromagnetic scattering. Figure 9 shows the ratio $F_2^{\mathrm{OTHER}}/F_2^{l^{\pm}}$ as a function of x for various charged lepton experiments [13–16], where $F_2^{l^{\pm}}$ is calculated from (13) using the F_2 measurement from this analysis. For each case, F_2 was extracted with the same R assumption that was used in the other analysis and the ratios were formed using only data in the overlapping Q^2 region. Apart from the EMC measurement, which has been scaled up in the Fig. by 10%, the level of agreement is quite good. The preliminary measurement from electron scattering using a deuterium target at SLAC was made at much lower energies ($E_e < 20$ GeV) than the other measurements with $R=0$ assumed. Results from EMC (μ – Fe; $R=R_{\mathrm{QCD}}$), BFP (μ – Fe; $R=0$) and BCDMS (μ – C; $R=R_{\mathrm{QCD}}$) were obtained using muon beams of comparable energy to this experiment.

4.3 Gross-Llewellyn Smith sum rule

In the QPM, the total number of valence quarks in the nucleon is equal to three. Identifying xF_3 as the momentum fraction carried by valence quarks, the GLS sum rule takes the form:

Table 3. Differences in assumptions used by various neutrino groups for structure function extraction. Also shown is the total event sums used in the structure function analysis. The two different parametrizations of R_{QCD} are:

$$R_{\mathrm{QCD}}^{[a]} = \frac{1.5(1-x)^4}{\ln(Q^2/0.04)},$$

$$R_{\mathrm{QCD}}^{[b]} = \frac{0.73(1-x)^{3.7}}{\ln(Q^2/0.058)}$$

	CCFR (89)	CCFRR (84)	CHARM (83)	CDHSW (87)	WA 59 (87)
Target	Fe	Fe	$CaCO_3$	Fe	Ne-H_2
ν's $\times 10^3$	88	59	50	565	8
$\bar{\nu}$'s $\times 10^3$	9	6	110	344	13
σ^{ν}/E (GeV/cm^2)	0.676	0.669	0.604	0.686	0.723
$\sigma^{\bar{\nu}}/E$ (GeV/cm^2)	0.333	0.340	0.301	0.339	0.351
κ	0.50	0.50	0.00	0.22	0.50
m_c GeV/c^2	1.5	1.5	0.0	0.0	1.5
$R=\sigma_L/\sigma_T$	$R_{\mathrm{QCD}}^{[a]}$	$R_{\mathrm{QCD}}^{[b]}$	0	$R_{\mathrm{QCD}}^{[a]}$	$R_{\mathrm{QCD}}^{[b]}$
Fermi motion	No	No	Yes	No	No

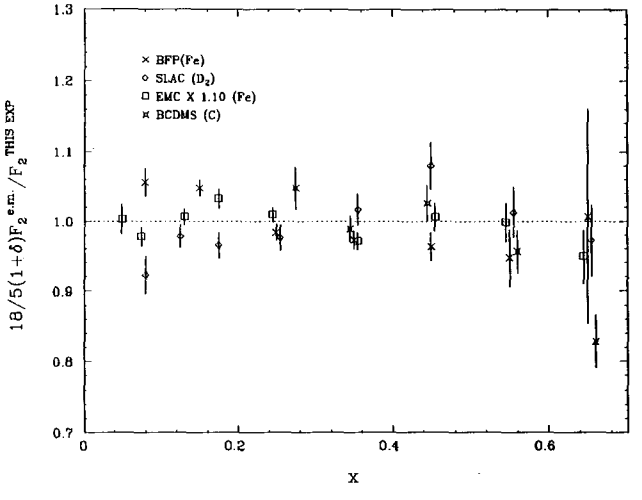

Fig. 9. The mean squared charge test: Ratio of F_2 measured in the charged lepton experiments and the predicted value

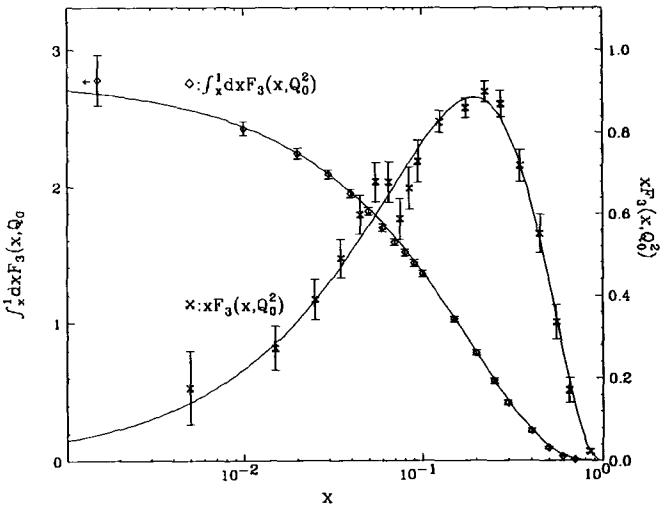

Fig. 10. The GLS sum rule: The crosses are xF_3 evaluated at $Q^2=3\,(\mathrm{GeV/c})^2$ (right scale) and the diamonds are the cumulative integrals

$$\int_0^1 \frac{dx}{x} xF_3(x,Q^2) = 3\left(1-\frac{a_S(Q^2)}{\pi}\right), \tag{14}$$

where the term in parantheses accounts for strong interaction effects predicted by QCD [17]. To test the QCD prediction in an optimal way, xF_3 was inter/extra-polated to a fixed value of Q^2. The $\frac{1}{x}$ weight amplifies the small x contribution to the sum rule: a region accessible only at small values of Q^2. To minimize the region of extrapolation, $Q_0^2=3\ \mathrm{GeV}^2$ was chosen.

The Q^2 interpolation (extrapolation for $x>0.15$, a region which constitutes only a third of the integral) used the Q^2 dependence predicted by QCD (dits to xF_3, discussed below, were used with $\Lambda_{\overline{MS}}=250$ MeV/c). In each x bin, the level of the QCD prediction was fit to the data and evaluated at Q_0^2. Uncertainties in Λ, which govern the Q^2 dependence, were translated into uncertainties in the interpolated or extrapolated values and added in quadrature to the statistical errors. To reduce the large statistical error from direct numerical integration of F_3, dominated by the lowest x point, the data were fitted to an x dependence given by:

$$xF_3(x,Q_0^2) = Ax^b(1-x)^c. \tag{15}$$

Figure 10 shows $xF_3(x,Q_0^2)$ (crosses) and the numerically evaluaed cumulative integral, $\int_0^x dx'\,F_3(x',Q_0^2)$ (diamonds) respectively. The solid curves are from the fit to the data yielding $\chi^2=15$ for 16 degrees of freedom. Integration of the fit provides

$$\int_0^1 \frac{dx}{x} xF_3(x,Q_0^2) = 2.78\pm0.08\pm0.13 \tag{16}$$

where the first error is statistical and the second is the quadrature sum of the systematic errors. The dominant contributions to the systematic errors include ±0.09 from the 3.1% correlated flux uncertainty and ±0.07 from the 1.7% uncorrelated flux uncertainty.

4.4 Scaling violations

The Altarelli-Parisi evolution equations [8] were used in this analysis to estimate the QCD scale parameter, Λ. The procedure involved parametrizing the x-dependence of the underlying parton momentum densities at some value of $Q^2=Q_0^2$. For a nucleon target, the relevant parton densities are the singlet, q^s, and nonsinglet, q^{ns}, quark densities (sum and difference of quark and antiquark densities respectively) and the gouon density, G. The Q^2 dependence of these parton densities was then evolved by integrating the Altarelli-Parisi equations,

$$\frac{dq^{ns}(x,Q^2)}{d\log Q^2} = \frac{\alpha_S(Q^2)}{2\pi}\int_x^1 \frac{dy}{y} q^{ns}(y,Q^2) P_{qq}^{ns}\left(\frac{x}{y},Q^2\right) \tag{17}$$

$$\frac{dq^s(x,Q^2)}{d\log Q^2} = \frac{\alpha_S(Q^2)}{2\pi}\int_x^1 \frac{dy}{y} \times\left(q^s(y,Q^2)P_{qq}^s\left(\frac{x}{y},Q^2\right) + G(y,Q^2)P_{qg}\left(\frac{x}{y},Q^2\right)\right) \tag{18}$$

$$\frac{dG(x,Q^2)}{d\log Q^2} = \frac{\alpha_S(Q^2)}{2\pi}\int_x^1 \frac{dy}{y} \times\left(q^s(y,Q^2)P_{gq}\left(\frac{x}{y},Q^2\right) + G(y,Q^2)P_{gg}\left(\frac{x}{y},Q^2\right)\right) \tag{19}$$

where the splitting functions, P_{qq}^{s}, P_{qq}^{ns}, P_{gq}, P_{qg} and P_{gg} are calculable perterbatively and $\alpha_S(Q^2)$ is the running quark-gluon coupling constant. At a given value of x, the Q^2 evolution of a parton density is governed both by α_S and the relevant parton densities at $x' > x$. Gluons in the nucleon with momentum fraction x at one value of $Q^2 = Q_0^2$ will contribute to the virtual $q\bar{q}$ sea through pair production with momentum fraction $x' < x$ at $Q_1^2 > Q_0^2$. Likewise at Q_0^2, quarks or antiquarks with momentum fraction, x, contribute the gluon content through gluon Bremsstrahlung with momentum fraction $x' < x$ at $Q^2 > Q_0^2$. In the nonsinglet case, the quark and antiquark couplings to the gluons cancel (17) depends only on q^{ns}), while in the singlet case they do not (18) and (19) are coupled).

To leading order in α_S, $F_2(x, Q^2) = q^s(x, Q^2)$ and $xF_3(x, Q^2) = q^{ns}(x, Q^2)$, that is, apart from the Q^2 dependence, QCD looks formally like the QPM. Beyond leading order, the relationship between the structure functions and parton densities is modified, but F_2 depends only on q^s and G while xF_3 depends only on q^{ns}.

A computer program based on one supplied by Duke and Owens [18] was used to perform fits to the next-to-leading order (NLO in the $\overline{MS}$ renormalization scheme) approximation of perturbative QCD*. The structure of the program was modified to allow for simultaneous fits to F_2 and xF_3 and to include the correlated errors.

Fits to xF_3 provide the cleanest means of confronting the predictions of QCD since its evolution is independent of the unmeasured gluon evolution. Furthermore, the extracted values of xF_3 are fairly insensitive to the assumed parametrizations of $R = \sigma_L/\sigma_T$ and the strange sea used in the structure function extraction. On the other hand, such an analysis is limited by the larger statistical errors implicit in measurements of xF_3. Interpretation of scaling violations in F_2 is complicated by the unmeasured gluon density; i.e. the observed scaling violations at a given value of x may be equally well described by a variety of different values of α_S and gluon densities at $x' > x$. At the same time, the measurement of the quark/antiquark sea from the difference between F_2 and xF_3 provides a constraint on the gluon density, especially at large x where the difference is small.

4.4.1 Fitting procedure. Data were compared to the QCD predictions by forming a χ^2 from the measured structure functions and those evolved through application of the Altarelli-Parisi equations. For simultaneous fits to F_2 and xF_3 the correlations were included. The χ^2 was minimized through the variation of Λ and the parameters of the relevant parton momentum densities (evaluated at Q_0^2). Inidividual contributions to the systematic errors on Λ were estimated by performing the χ^2 minimizations on data sets with structure function values shifted from their nominal values by the estimated sytematic uncertainties given in Table 2.

Predictions of perturbative QCD are expected to be valid in the limit of large Q^2. Logarithmic scaling violations are a consequence of "leading twist" operators in the operator product expansion [19]. Higher twist operators, which contribute to scaling violations with strengths proportional to inverse powers of Q^2, dominate the leading twist behavior below some unknown, but small, value of Q^2. It would be desirable to impose a large Q^2 cut to eliminate this region, however the limited statistics and available range of Q^2 require some compromise. In all fits, only data above $Q^2 = 6\,(\mathrm{GeV/c})^2$ were used. Barnett has suggested [20] that the most appropriate quantity for describing non-perturbative effects is the invariant hadronic mass, $W^2 = M^2 + Q^2(1-x)/x$. Again, with statistical and kinematic limitations in mind, only data with $W^2 > 10\,\mathrm{GeV}^2$ were used in the fits. Finally, data with $x > 0.7$ were unused since experimental corrections (resolution smearing and bin center) are large and unreliably modelled. The kinematic cuts are summarized here:

$$Q^2 > 6\,(\mathrm{GeV/c})^2 \quad 0.03 < x < 0.70$$

$$W^2 > 10\,\mathrm{GeV}^2 .$$

The minimum x cut is a consequence of the Q^2 cut, but is shown explicitly. A total of 48 F_2 and xF_3 data points passed the cuts.

Fits were performed both with and without target mass corrections using the prescription of Georgi and Politzer [22]. Differences in the evolved structure functions appear at large values of $4M^2x^2/Q^2$, a region eliminated by the x and W^2 cuts. Since the fit values of Λ obtained with and without application of the target mass correction differed by a small fraction of the statistical error, it was concluded that target mass effects are unimportant in this analysis. All results are reported without this correction applied.

All parton momentum densities were parametrized at $Q_0^2 = 1\,(\mathrm{GeV/c})^2$. The validity of perturbation theory at such low values is not an issue since only densities evolved to $Q^2 > 6\,(\mathrm{GeV/c})^2$ were used in the fits. The nonsinglet parametrization is given by:

$$q_{ns}(x, Q_0^2) = A_{ns}\, x^{\eta_1}(1-x)^{\eta_2}(1+\gamma x), \tag{20}$$

where A_{ns} was fixed by the fermion conservation rule

$$\int_0^1 \frac{dx}{x}\, q_{ns}(x, Q_0^2) = 3 . \tag{21}$$

Fermion conservation is a built-in feature of the nonsinglet operator in the factorization scheme used, valid to all orders of perturbation theory. A numerical check on the evolved nonsinglet density showed that (21) was satisfied at the 1% level for $1 < Q^2 < 300\,(\mathrm{GeV/c})^2$.

The singlet fits required parametrizations of both the singlet quark momentum density and the gluon momentum density:

$$q_s(x, Q^2) = q_{ns}(x, Q^2) + B_s(1-x)^{\eta_s} \tag{22}$$

$$G(x, Q^2) = A_g(1-x)^{\eta_g}(1+\gamma_g x), \tag{23}$$

* Minor coding errors found in the next-to-leading order splitting functions and coefficient functions were detected and corrected

where A_g was fixed by the momentum sum rule:

$$\int_0^1 dx[q_s(x,Q_0^2)+G(x,Q_0^2)]=1. \quad (24)$$

4.4.2 Nonsinglet fit results. The results of the nonsinglet NLO fits are shown in Table 4 and Fig. 7a shows the fits superimposed on the data. The systematic errors in Λ and α_S, at $Q^2=12.6\,(\mathrm{GeV/c})^2$ (the geometric mean Q^2 value of this experiment) are listed in Table 5. The results of the nonsinglet fits are summarized here.

$$\Lambda_{\overline{MS}}=251\,^{+134}_{-115}\pm 89\ \mathrm{MeV/c} \quad (25)$$

$$\alpha_S=0.222\pm 0.037\pm 0.026$$

$$\text{at } Q^2=1.6\,(\mathrm{GeV/c})^2. \quad (26)$$

The errors are statistical followed by systematic. We quote the later since the value of α_S is reasonably linear in the observables, so that the errors are nearly symmetric. The systematic errors on $\Lambda_{\overline{MS}}$ were obtained by adding the systematic errors in α_S in quadrature and obtaining the corresponding value of Λ. The next-to-leading order value of α_S was found in all calculations by numerically inverting

$$\ln(Q^2/\Lambda^2_{\overline{MS}})=\frac{4\pi}{\beta_0\alpha_S}-\frac{\beta_1}{\beta_0^2}\ln\left[\frac{4\pi}{\beta_0\alpha_S}+\frac{\beta_1}{\beta_0^2}\right], \quad (27)$$

where,

$$\beta_0=11-\tfrac{2}{3}N_f$$
$$\beta_1=102-\tfrac{38}{3}N_f, \quad (28)$$

and the number of flavors was fixed at $N_f=4$.

The comparison shown in Fig. 7a indicates that the fit is consistent with the data. Another way of displaying the level of agreement between theory and measurement is through a direct comparison of the scaling violations. Since both the data and the fits are consistent with a power law dependence in Q^2 at a fixed x, the logarithmic derivatives are consistent with being independent of Q^2:

$$\frac{d\ln xF_3(x,Q^2)}{d\ln Q^2}\approx A(x). \quad (29)$$

Figure 11 shows the measured xF_3 slopes (crosses) calculated in each x bin from fits of the form: $xF_3=a(Q^2)^b$. The predicted slopes (lines) were calculated by fitting the predicted structure functions, evaluated at the same Q^2 values as the data, to the same functional form, using the measured errors. The solid (upper dashed; lower dashed) curve is a smooth interpolation of the predicted slopes for $\Lambda_{\overline{MS}}=251$ (96; 437) MeV/c.

The measured scaling violations in the highest x bins appear larger than the predicted values, although the statistical significance is not compelling. If one assumes that $F_2\approx xF_3$ for $x>0.4$ (diamonds in Fig. 11) to be valid (equivalent to the assumption that gluons and sea quarks can legitimately be ignored at high x), then the statistical errors become smaller but the trend persists. Results of

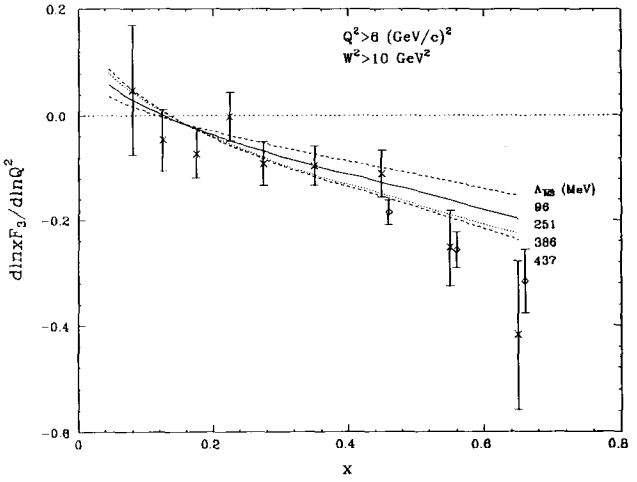

Fig. 11. Logarithmic derivatives of xF_3 (crosses) and $(1+Q^2/\nu^2)/(1+R)F_2$ (diamonds) along with predictions from the NLO nonsinglet fits. The solid line corresponds to the $\Lambda_{\overline{MS}}=251$ MeV/c fit to xF_3 and the dotted line corresponds to the $\Lambda_{\overline{MS}}=386$ MeV/c fit to $xF_3(x<0.40)$ and $F_2(x>0.40)$. The dashed lines are the $\pm 2\sigma$ predictions: 96 MeV/c (shallow line) and 437 MeV/c (steep line)

Table 4. Nonsinglet fit results for next to leading order QCD. Column labeled F_2 and xF_3 shows results for use of F_2 above $x=0.4$

Parameter	Nonsinglet fit	
	xF_3	F_2 and xF_3
Λ (MeV)	$251\,^{+134}_{-115}$	$386\,^{+78}_{-74}$
η_1	0.828 ± 0.032	0.944 ± 0.014
η_2	$3.66\ \pm 0.14$	$2.79\ \pm 0.09$
γ	$0.67\ \pm 0.39$	$-0.57\ \pm 0.14$
χ^2/dof	48.0/44	46.5/44
α_S 12.6 $(\mathrm{GeV/c})^2$	0.222 ± 0.037	0.259 ± 0.020

Table 5. Contributions to the systematic errors in Λ_{LO} and $\Lambda_{\overline{MS}}$ from the nonsinglet fits. $R_{\mathrm{QCD}}-0$ indicates difference between structure functions extracted assuming $R=R_{\mathrm{QCD}}$ and $R=0$

System	Δ (System)	$\overline{MS}$	
		$\Delta\Lambda_{\overline{MS}}$ (MeV)	$\Delta\alpha_S$
E_{had}	+ 1%	− 57	−0.017
E_μ	+ 1%	+ 2	+0.001
All E	+ 1%	− 2	−0.001
$P_{\mathrm{sec}\,y}$	+ 1%	+ 56	+0.016
$\sigma_{\theta_{\mathrm{sec}\,y}}$	+10%	− 3	−0.001
$\Phi^{\bar{\nu}}/\Phi^{\nu}$	+ 1.7%	+ 1	−
$(\Phi^{\bar{\nu}}+\Phi^{\nu})$	+ 3.2%	+ 36	+0.010
R	$R_{\mathrm{QCD}}-0$	+ 28	+0.008
Total		± 89	±0.026
Stat		±124	±0.037

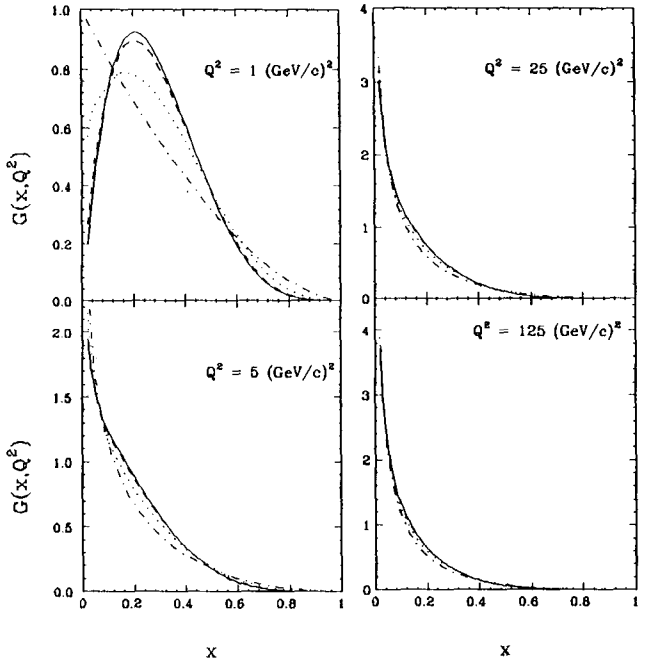

Fig. 12. Gluon densities for various values of Q^2 and γ_g: $\gamma_g = 0$ (dot-dashed), 10 (dotted), 100 (dashed) and 10^6 (solid)

fits to xF_3 for $x < 0.4$ and $(1+Q^2/\nu^2)/(1+R)F_2$ for $x > 0.4$ yielded:

$$\Lambda_{\overline{MS}} = 386^{+78}_{-74}\ \text{MeV/c}, \tag{30}$$

where the errors are statistical only, and other parameters are listed in Table 4. It should be noted that this replacement of F_2 for xF_3 is not quite valid in principle in the NLO case, due to the different coefficient functions relating the quark density to F_2 and xF_3.

4.4.3 Singlet fit results. Two separate types of singlet fits to the data have been performed. The first method involved fitting only F_2 to the Altarelli-Parisi equations. In the second method, F_2 and xF_3 were simultaneously fit to the Altarelli-Parisi equations. For the latter case, $q_{ns}(x, Q_0^2)$ and $q_s(x, Q_0^2)$ were separately evolved with their respective splitting kernels.

Both types of fits yielded very hard gluon densities at Q_0^2 (relatively large fraction at high x.) When γ_g in (23) was left a free parameter, it converged to a very large value. The resulting $G(x, Q_0^2)$ was peaked at $x \sim 0.2$. Figure 12 shows $G(x, Q^2)$ from fits to F_2 at various values of Q^2 for values of $\gamma_g = 0, 10, 10^2$ and 10^6 and fixed $\Lambda_{\overline{MS}} = 250$ MeV/c (see below). The preferred gluon densities, at large γ_g, are large at intermediate values of x. By $Q^2 = 5$ (GeV/c)^2, all of the gluon momentum densities have begun to decrease with increasing x as intuitively expected.

Figure 13 shows values of χ^2 contours for the F_2 fits as a function of $\Lambda_{\overline{MS}}$ for the different values of γ_g. Since the best value of $\Lambda_{\overline{MS}}$ is insensitive to the choice of γ_g, the gluon densities shown in Fig. 12 are "best fits." All subsequent singlet fits were performed with $\gamma_g = 10^6$ fixed.

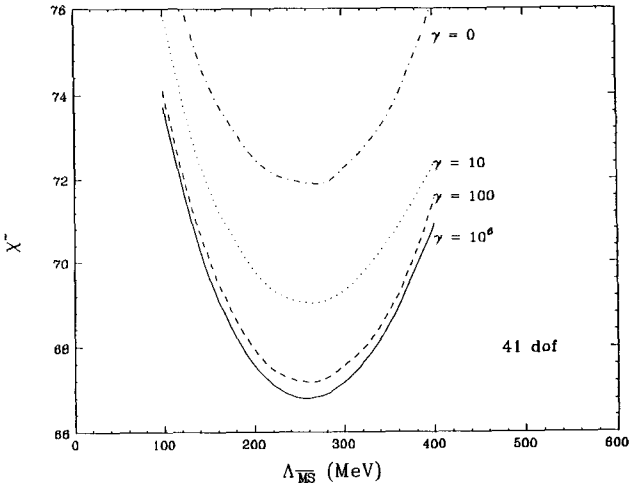

Fig. 13. χ^2 contours as a function of $\Lambda_{\overline{MS}}$ for NLO fits to F_2 alone: $\gamma_g = 0$ (dot-dashed), 10 (dotted), 100 (dashed) and 10^6 (solid)

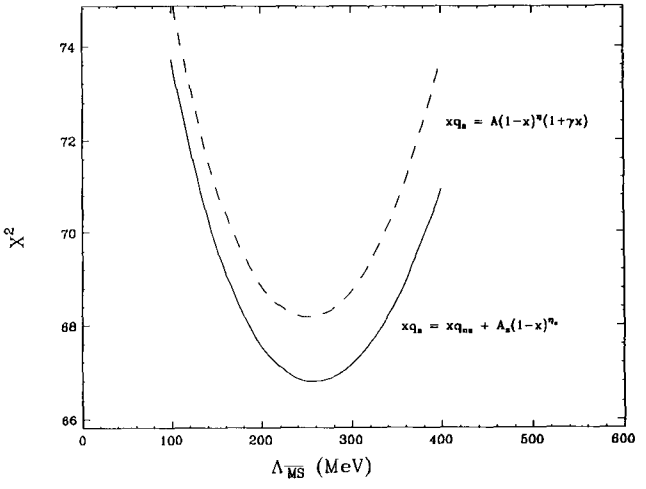

Fig. 14. χ^2 contours as a function of $\Lambda_{\overline{MS}}$ for NLO fits to F_2 alone, using different Q_0^2 parametrizations of the singlet quark density

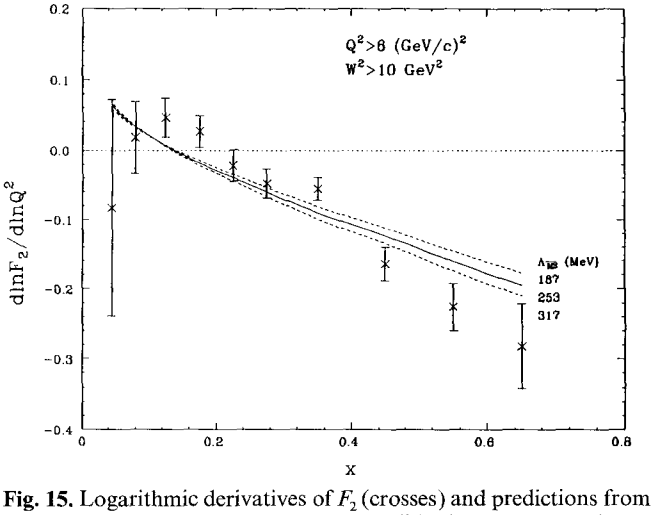

Fig. 15. Logarithmic derivatives of F_2 (crosses) and predictions from the NLO simultaneous fits. The solid line corresponds to $\Lambda_{\overline{MS}} = 253$ MeV/c. The dashed lines are the $\pm 2\sigma$ predictions: 187 MeV/c (shallow line) and 317 MeV/c (steep line)

Table 6. Results of NLO fit to F_2 alone and the simultaneous F_2 and xF_3 fit

Parameter	MS singlet fit		
	$q_s = A_s(1-x)^{\eta_2}(1+\gamma x)$	$q_s = q_{ns} + B_s(1-x)^{\eta_s}$	
	F_2	F_2	F_2 and xF_3
$\Lambda_{\overline{MS}}$ (MeV)	244^{+71}_{-54}	255^{+73}_{-63}	253^{+55}_{-50}
η_1	–	0.823 ± 0.020	0.865 ± 0.017
η_2	3.162 ± 0.054	2.678 ± 0.039	2.887 ± 0.033
γ	4.764 ± 0.806	-0.674 ± 0.032	-0.593 ± 0.027
A_s	1.334 ± 0.083	–	–
B_s	–	1.103 ± 0.081	1.271 ± 0.160
η_s	–	7.435 ± 0.294	8.983 ± 1.167
η_g	3.695 ± 0.973	3.720 ± 1.413	4.131 ± 1.139
χ^2/dof	68.1/43	66.8/41	116/89
α_S 12.6 (GeV/c)^2	0.220 ± 0.018	0.223 ± 0.020	0.223 ± 0.015

Table 7. Contributions to the systematic errors in $\Lambda_{\overline{MS}}$ for the fits shown in Table 6

System	Δ (System)	F_2		F_2 and xF_3	
		$\Delta\Lambda_{\overline{MS}}$ (MeV)	$\Delta\alpha_S$	$\Delta\Lambda_{\overline{MS}}$ (MeV)	$\Delta\alpha_S$
E_{had}	+ 1%	− 61	−0.018	−44	−0.015
E_μ	+ 1%	+ 5	+0.002	+ 5	+0.001
All E	+ 1%	+ 7	+0.002	− 8	−0.002
$P_{sec\,y}$	+ 1%	+ 77	+0.022	+36	+0.010
$\sigma_{\theta_{sec\,y}}$	+10%	+ 10	+0.003	−10	−0.003
$\Phi^{\bar{\nu}}/\Phi^{\nu}$	+ 1.7%	− 13	−0.004	−21	−0.006
$(\Phi^{\bar{\nu}} + \Phi^{\nu})$	+ 3.2%	+ 20	+0.006	+28	+0.008
Total		±101	±0.030	±71	±0.021
Stat		± 68	±0.020	±53	±0.015

The parametrization shown in (22) was utilized for simultaneous fits when both the singlet and nonsinglet quark densities were evolved. For fits to F_2 alone, a standard Q_0^2-parametrization of the singlet quark density was also tried:

$$q_s(x, Q_0^2) = A_s(1-x)^{\eta_2}(1+\gamma x) \tag{31}$$

where A_s, η_2 and γ were unconstrained, apart from the momentum sum rule. Figure 14 shows the χ^2 contours as a function of $\Lambda_{\overline{MS}}$ for the two different singlet quark parametrizations. The best values of $\Lambda_{\overline{MS}}$ and η_g are consistent for the two cases.

The results of the NLO singlet fits are shown in Table 6. Figure 7b shows the best fit to F_2 superimposed on the data. The large χ^2's indicate that either the data are only consistent with perturbative QCD at the three sigma level, or that the systematic errors are significant. Table 7 lists the contributions to the systematic errors in $\Lambda_{\overline{MS}}$ and α_S (using $q_s(x, Q_0^2)$ given in (22), indicating that the systematic errors are significant. When all systematic errors on F_2, apart from the correlated flux uncertainty which only affects the overall level, are added in quadrature to the statistical errors, the χ^2 decreases from 66.8 for 41 degrees of freedom (dof) to 47.6/41 dof indicating a good fit. In thise case, the central value of $\Lambda_{\overline{MS}}$ also decreases by 30 MeV/c, well within the quoted systematic error. This can be understood from Fig. 15 which shows the comparison between the measured and predicted scaling violations as a function of x. The large measured scaling violations at large x tend to force Λ to larger values. Since the systematic errors are largest in this region, the relative contribution to the χ^2 from these degrees of freedom was reduced. Figures 11 and 15 both suggest that at large values of x, scaling violations predicted by QCD are smaller than measured scaling violations. The F_2 comparison indicates that in the region $0.1 < x < 0.4$, the measured scaling violations lie above the QCD predictions.

Also shown in Tables 6 and 7 are the results of the simultaneous fits F_2 and xF_3. Figure 16 shows the χ^2 contours as a function of $\Lambda_{\overline{MS}}$ for the simultaneous fit, along with the nonsinglet fit, and the F_2 (q_s given in (22)) fir for comparison. As was the case for the other NLO fits discussed, the dominant systematic error arises from the hadron energy and neutrino energy calibrations. The determination of $\Lambda_{\overline{MS}}$ from the simultaneous fit is limited by these systematic errors. Adding the structure functions' systematic errors in quadrature with their statistical errors resulted in a reduction of the χ^2 from 116/89 dof to 92/89 dof with a corresponding reduction in $\Lambda_{\overline{MS}}$ of 35 MeV/c.

The quality of the simultaneous fits is in good agreement with both the nonsinglet and singlet (F_2 only) fits:

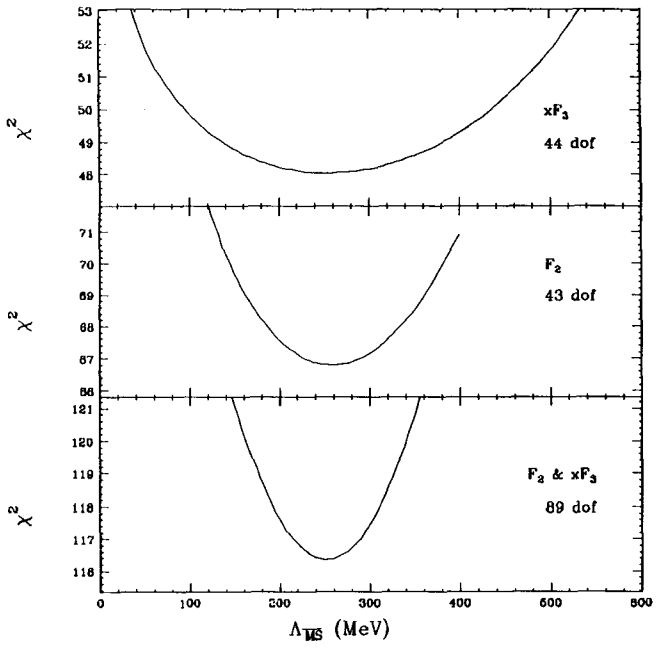

Fig. 16. χ^2 contours as a function of $\Lambda_{\overline{MS}}$ for the NLO nonsinglet, F_2 only, and simultaneous fits to F_2 and xF_3

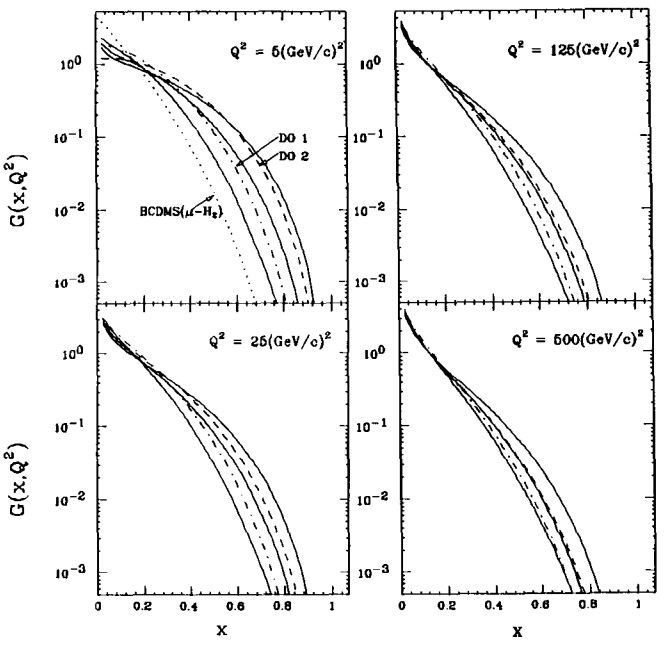

Fig. 17. Gluon densities for NLO simultaneous fits at various Q^2 values. The solid lines correspond to $\eta_g = 4.13$, 2.80 and 6.50, the best (center lines), -2σ (hard) and $+2\sigma$ (soft) values. The dashed and dotted lines are the hard and soft densities from [23] and the dotted line is from [24]

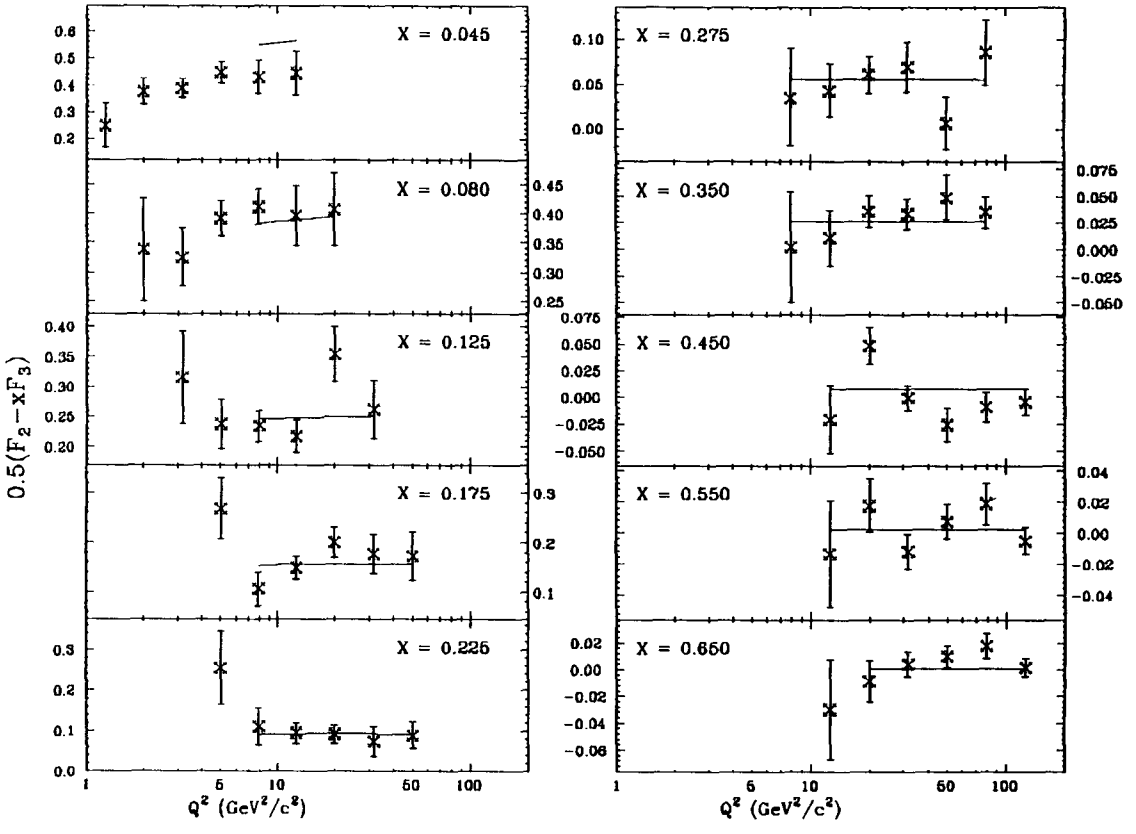

Fig. 18. $\bar{q} \sim 0.5[F_2 - xF_3]$ and the NLO simultaneous fit described in text

Considering only the F_2 degrees of freedom, the simultaneous fit yielded a χ^2 of 69.1 as compared to 66.8 for the fit to F_2 alone. The xF_3 degrees of freedom for the simultaneous fit yielded a χ^2 of 52.0 as compared to 48.0 for the nonsinglet fit. Another check on the consistency of the fits came from comparing the F_2 fits to xF_3. When the nonsinglet part of the F_2 fit, $q_{\rm ns}(x, Q_0^2)$ in (22), was evolved by itself and compared with xF_3, the resulting χ^2 was 59.4 for 48 degrees of freedom as compared to 48/44.

Figure 17 shows the gluon momentum densities at different values of Q^2 for $\eta_g = 4.13$, 6.50 and 2.80 (see (23)), corresponding to the best value and $\pm 2\sigma$ ($\Lambda_{\overline{MS}} = 253$, 265 and 225 MeV/c respectively). Also shown on these plots are the "soft" (DO 1: $\Lambda_{\overline{MS}} = 200$ MeV/c) and "hard" (DO 2: $\Lambda_{\overline{MS}} = 400$ MeV/c) gluon densities given in [23]. At large values of x, the best gluon density from this analysis lies between their two extremes. The $Q^2 = 5\,(\mathrm{GeV/c})^2$ plot also shows the gluon density extracted by the BCDMS collaboration using a hydrogen target [24] with $\Lambda_{\overline{MS}} = 220$ MeV/c. This gluon density is inconsistent with the others shown. In fact, BCDMS makes use of their soft gluon density to justify the claim that above $x = 0.25$ and $Q^2 = 20\,(\mathrm{GeV/c})^2$, F_2 is approximately nonsinglet [25]. Figure 18 shows the difference $0.5\,(F_2 - xF_3) \sim x\bar{q}$, along with the simultaneous NLO fit shown in Table 7. Both the hard gluon distribution obtained and the substantial antiquark density at large x show that approximating the nonsinglet density with F_2 below $x = 0.4$ is a questionable procedure.

5 Conclusions

Structure functions extracted from data obtained in two narrow band neutrino and antineutrino exposures at Fermilab have been presented. These results are in reasonable agreement with high statistics results from wide band exposures from neutrino experiments at CERN. In particular, the level of agreement between data from this analysis and the recent CDHSW results has improved greatly. The quark parton model tests provide consistency checks on the data. Apart from an overall 10% level difference between the results reported here and those from EMC, the mean square charge test demonstrated consistency at few percent level for several charged lepton scattering experiments. The measurement of the Gross-Llewellyn Smith sum rule is:

$$\int_0^1 \mathrm{d}x F_3(x, 3\,(\mathrm{GeV/c})^2) = 2.78 \pm 0.08 \pm 0.13\,. \tag{32}$$

The value is consistent with the theoretical prediction.

Measured deviations from scaling predicted by the QPM were analysed in the context of perturbative QCD. Three types fits to the Altarelli-Parisi equations were performed. A purely nonsinglet fit to xF_3 yielded:

$$\Lambda_{\overline{MS}} = 251\,^{+134}_{-115} \pm 89 \text{ MeV/c} \tag{33}$$

$$\alpha_S = 0.222 \pm 0.037 \pm 0.026 \quad \text{at } Q^2 = 12.6\,(\mathrm{GeV/c})^2\,. \tag{34}$$

This value of $\Lambda_{\overline{MS}}$, obtained at large Q^2, is consistent with the value predicted from the GLS sum rule at lower Q^2. Singlet fits were performed using F_2 alone and using both F_2 and xF_3 simultaneously. The results of these fits were consistent with the purely nonsinglet fits:

$$\left.\begin{aligned} \Lambda_{\overline{MS}} &= 255\,^{+73}_{-63} \pm 101 \text{ MeV/c} \\ \alpha_S &= 0.223 \pm 0.020 \pm 0.030 \\ &\text{at } Q^2 = 12.6\,(\mathrm{GeV/c})^2 \end{aligned}\right\} F_2 \text{ Only}$$

$$\left.\begin{aligned} \Lambda_{\overline{MS}} &= 253\,^{+55}_{-50} \pm 71 \text{ MeV/c} \\ \alpha_S &= 0.223 \pm 0.015 \pm 0.021 \\ &\text{at } Q^2 = 12.6\,(\mathrm{GeV/c})^2 \end{aligned}\right\} F_2 \text{ and } xF_3\,. \tag{35}$$

The coupling of the singlet quark density evolution to the gluon evolution was used to constrain the gluon density shape. It was found that the conventional parametrization for the gluons, $xG(x, Q_0^2) = A(1-x)^{\eta_g} \cdot (1 + \gamma_g x)$, provided a good description of the data only when a low value of Q_0^2 was chosen. The resulting gluon density was found to be harder than that reported by the BCDMS collaboration. The best gluon result from this analysis lies between the hard and soft densities given by Duke and Owens [23] for x above 0.2 (high Q^2) to 0.4 (low Q^2).

Appendix A. Differential cross section model corrections

Six structure functions, $2x\mathscr{F}_1^{\nu(\bar{\nu})}$, $\mathscr{F}_2^{\nu(\bar{\nu})}$, and $x\mathscr{F}_3^{\nu(\bar{\nu})}$, were used to parametrize the $\nu\,(\bar{\nu})$-Fe differential cross sections. These structure functions were expressed in terms of bare parton momentum densities for up and down valence quarks and sea quarks in the proton, $u_v(x, Q^2)$, $d_v(x, Q^2)$ and $S(x, Q^2)$. These parton densities were fit to the extracted structure functions at each stage of iteration through the relations

$$F_2(x, Q^2) = \frac{1 + R(x, Q^2)}{1 + 4M^2x^2/Q^2}\,[u_v(x, Q^2) + d_v(x, Q^2) + S(x, Q^2)] \tag{36}$$

$$xF_3(x, Q^2) = [u_v(x, Q^2) + d_v(x, Q^2)] \tag{37}$$

where $R(x, Q^2) = 1.5\,(1-x)^4/\log(Q^2/0.04)$ was assumed. The following assumptions were employed in the parton density parametrizations:

- Strong isospin symmetry was assumed: $d_v(x, Q^2)$ of the proton is functionally identical to $u_v^n(x, Q^2)$, the valence up content of the neutron.
- Valence down quarks in the proton were assumed to fall faster then valence up quaks at large x: $d_v/u_v \sim (1-x)$.

The relative d_v to u_v normalizations were fixed by assuming $\int \frac{dx}{x} u_v(x, Q^2) = 2 \int \frac{dx}{x} d_v(x, Q^2)$. No overall normalization was imposed.

- The sea was assumed to be comprised of u, d and s quarks and antiquarks only. Furthermore, all flavors were parametrized using the same functional x and Q^2 dependence. The relative normalization of strange quarks to up or down quarks in the sea was taken to be 0.5 [26].

The neutron excess over protons in an iron target, the strange-charm asymmetry in the sea and the cross section suppression due to charm production results in $\mathscr{F}_i^{\nu} \neq \mathscr{F}_i^{\bar{\nu}}$. The procedure for "correcting" the reported structure functions for these effects is embodied in the calculation of $\delta^{\nu(\bar{\nu})}$ in (8) and (9). For neutrino scattering,

$$\delta^{\nu}(x_0, Q_0, E)$$

$$= Ey \left[\frac{y^2}{2} \left(2x\mathscr{F}_1^{\nu} - \frac{1+4M^2x^2/Q^2}{1+R} F_2 \right) \right. \tag{38}$$

$$+ \left(1 - y - \frac{Mxy}{2E} \right) (\mathscr{F}_2^{\nu} - F_2) \tag{39}$$

$$\left. + \left(y - \frac{y^2}{2} \right) (x\mathscr{F}_3^{\nu} - xF_3) \right]; \tag{40}$$

and $\delta^{\bar{\nu}}$ is given by an analogous expression. The $\mathscr{F}_i$ appearing here were expressed in terms of $q^{\nu(\bar{\nu})}$ and $\bar{q}^{\nu(\bar{\nu})}$, the quark and antiquark momentum densities probed by neutrinos (antineutrinos):

$$2x\mathscr{F}_1^{\nu}(x) = q_{ncp}^{\nu}(x) + \bar{q}^{\nu}(x) + \frac{x}{\xi} q_{cp}^{\nu}(\xi) \tag{41}$$

$$2x\mathscr{F}_1^{\bar{\nu}}(x) = q^{\bar{\nu}}(x) + \bar{q}_{ncp}^{\bar{\nu}}(x) + \frac{x}{\xi} \bar{q}_{cp}^{\bar{\nu}}(\xi) \tag{42}$$

$$\mathscr{F}_2^{\nu} = \frac{1+R(x)}{1+4M^2x^2/Q^2} (q_{ncp}^{\nu}(x) + \bar{q}^{\nu}(x)) + \frac{1+R(\xi)}{1+4M^2\xi^2/Q^2} q_{cp}^{\nu}(\xi) \tag{43}$$

$$\mathscr{F}_2^{\bar{\nu}} = \frac{1+R(x)}{1+4M^2x^2/Q^2} (q^{\bar{\nu}}(x) + \bar{q}_{ncp}^{\bar{\nu}}(x)) + \frac{1+R(\xi)}{1+4M^2\xi^2/Q^2} \bar{q}_{cp}^{\bar{\nu}}(\xi) \tag{44}$$

$$x\mathscr{F}_3^{\nu}(x) = q_{ncp}^{\nu}(x) - \bar{q}^{\nu}(x) + \frac{x}{\xi} q_{cp}^{\nu}(\xi) \tag{45}$$

$$x\mathscr{F}_3^{\bar{\nu}}(x) = q^{\bar{\nu}}(x) - \bar{q}_{ncp}^{\bar{\nu}}(x) - \frac{x}{\xi} \bar{q}_{cp}^{\bar{\nu}}(\xi) \tag{46}$$

where the Q^2 dependence has been suppressed. The subscripts *ncp* and *cp* refer to charm-producing and non-charm-producing flavors. Since antineutrinos cannot produce charm from scattering off quarks, there is no distinction made for $q^{\bar{\nu}}$. The slow rescaling [27] variable $\xi = x\left(1 + \frac{m_c^2}{Q^2}\right)$, appearing in conjunction with the charm-producing pieces, was used to simulate the threshold behavior with $m_c = 1.5\ (\mathrm{GeV/c})^2$.

The momentum densities appearing above were expressed in terms of the bare parton densities as follows:

$$q_{ncp}^{\nu} = \left((1-\alpha) d_v + (1+\alpha) u_v + \frac{S}{2+\kappa} \right) \times \cos^2\theta_C + \frac{\kappa}{2+\kappa} S \sin^2\theta_C \tag{47}$$

$$q_{cp}^{\nu} = \left((1-\alpha) d_v + (1+\alpha) u_v + \frac{S}{2+\kappa} \right) \times \sin^2\theta_C + \frac{\kappa}{2+\kappa} S \cos^2\theta_C \tag{48}$$

$$\bar{q}^{\nu} = \frac{1}{2+\kappa} S \tag{49}$$

$$q^{\bar{\nu}} = (1+\alpha) d_v + (1-\alpha) u_v + \frac{1}{2+\kappa} S \tag{50}$$

$$\bar{q}_{ncp}^{\bar{\nu}} = \frac{1}{2+\kappa} S \cos^2\theta_C + \frac{\kappa}{2+\kappa} S \sin^2\theta_C \tag{51}$$

$$\bar{q}_{cp}^{\bar{\nu}} = \frac{1}{2+\kappa} S \sin^2\theta_C + \frac{\kappa}{2+\kappa} S \cos^2\theta_C \tag{52}$$

Here $\alpha \equiv 1 - \left(\frac{2Z}{A}\right)_{Fe} = 0.0689$ is the isoscalar factor for iron, $\kappa = 0.5$ is normalization of s quarks relative to u or d quarks in the sea, and $\theta_C = 13.2°$ is the Cabibbo angle.

Appendix B. Absolute flux normalization

A parallel event analysis, using the same fiducial and beam cuts employed in the structure function analysis, was carried out to establish the relative neutrino to antineutrino flux level and overall level. By relaxing the kinematic cuts and making use of the dichromatic beam's energy-radius correlation, the (as yet) unnormalized differential cross sections,

$$\left\langle \frac{1}{E} \frac{d\sigma^{\nu(\bar{\nu})}}{dy} \right\rangle_{\nu(\bar{\nu})} (y), \tag{53}$$

were obtained over most of the kinematic range $0 < y < 1$. Their y-integrals were then compared directly with the total cross section slopes previously reported by this collaboration [28],

$$\begin{aligned} \sigma^{\nu}/E &= (0.669 \pm 0.003 \pm 0.024) \cdot 10^{-38}\ \mathrm{cm^2/GeV} \\ \sigma^{\bar{\nu}}/E &= (0.340 \pm 0.003 \pm 0.020) \cdot 10^{-38}\ \mathrm{cm^2/GeV}. \end{aligned} \tag{54}$$

This comparison provided a 3.5% constraint on the relative neutrino to antineutrino flux normalization (error

due to uncorrelated neutrino to antineutrino flux uncertainty) and a 3.1% constraint on the overall level (error due to correlated uncertainty).

The other constraint followed from a comparison of the low-y limits of the differential cross sections for neutrinos and antineutrinos. Formal integration of the double differential cross section over x at fixed $\nu = Ey$ gives

$$\lim_{y\to 0} \frac{1}{E}\frac{d\sigma}{dy} = \frac{G^2 M}{\pi}\int_0^1 dx F_2(x, Q^2=0). \tag{55}$$

To the extent that flavor asymmetries in the nucleon can be ignored, the "y-intercept" is independent of neutrino helicity and energy.

For this analysis, the 10 GeV hadron energy cut was removed*, extending the kinematic range to $y=0$. Penetration triggers were included in this analysis, extending θ_μ out to 370 mrad and E_μ down to 2.9 GeV. The y-value of events not fully reconstructed were determined from the dichromatic energy predicted by the energy-radius correlation. This required their classification as pion or kaon induced. The large energy separation between pion and kaon induced events, at a given radius, allowed the identification of events with $E_{had} > 0.85\,E^{SEP}(r)$ as kaon induced. The high muon trigger efficiency for kaon induced events with $E_{had} < 0.85\,E^{SEP}(r)$ and high penetration efficiency for all events with $E_{had} > 10$ GeV provided a statistical means of classifying events in this intermediate E_{had} range. Virtually all events with $E_{had} < 10$ GeV satisfied the muon trigger and y was computed from the measured energy.

Flux averaged differential cross sections, corrected for resolution smearing, reconstruction efficiency, geometric acceptance and bin center effects, were calculated in analogy to (11):

$$\left\langle \frac{1}{E}\frac{d\sigma^{\nu(\bar\nu)}}{dy}\right\rangle^{meas}_{\nu(\bar\nu)}(y_0) = \frac{N^{\nu(\bar\nu)}_{obs}}{N^{\nu(\bar\nu)}_{pred}}\left\langle \frac{1}{E}\frac{d\sigma^{\nu(\bar\nu)}_0}{dy}\right\rangle_{\nu(\bar\nu)}(y_0), \tag{56}$$

where the *relative* (setting to setting) contributions to N^{ν}_{pred} and $N^{\bar\nu}_{pred}$ were determined using the technique discussed in Sect. 3.1. Here, σ_0 is the model cross section with both radiative and non-isoscalar (but not W propagator) effects removed. This is because comparisons are made to the reported total cross section slopes which are corrected only for non-isoscalar effects. Radiative corrections affect the shape, not the level of the differential cross section, and thus have no bearing on the integral comparison.

The y-intercept constraint was applied by fitting the y-dependence of the differential cross sections to the form $A + B(1-y)^2$ in the interval $0.05 < y < 0.80$ and extrapolating to $y=0$. Data below $y=0.05$ wer not used in the fits since quasi-elastic like processes**,which do not scale with energy, are important. Figure 19 shows the normalized neutrino and antineutrino y-distributions along with the fits described above.

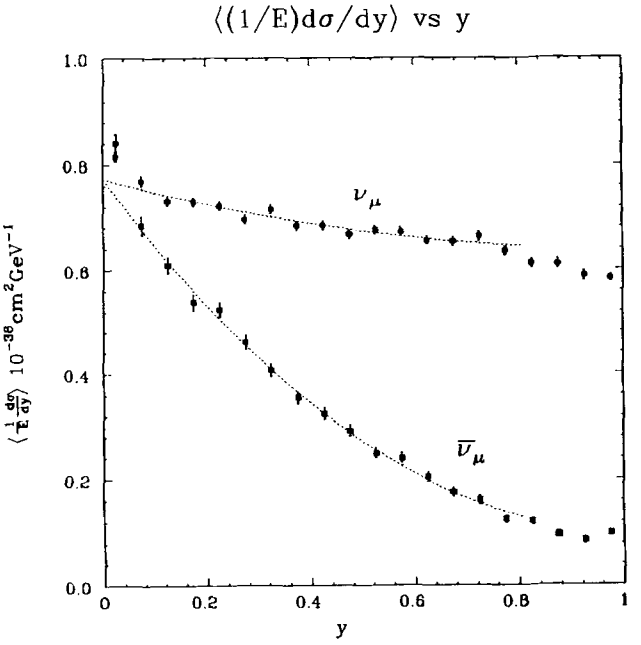

Fig. 19. Normalized neutrino (circles) and antineutrino (squares) differential cross sections corrected for radiative and isoscalar effects only. The solid lines are fits to the $A + B(1-y)^2$

A Monte Carlo calculation was used to estimate the different between neutrino and antineutrino y-intercepts due to charm production and the strange sea asymmetries. It was also used to estimate extrapolation errors due to uncertainties in $R = \sigma_L/\sigma_T$ and scaling violations. Since only the ratios of the y-intercepts are relevant, much of the systematic uncertainty cancels. The predicted value of the neutrino to antineutrino y-intercept ratio was found to be 1.012 ± 0.015 where the error is due to systematic uncertainties in the charm quark mass, R and strange sea fraction. Combined with a 1.3% statistical error on the measured ratio, this technique provided a 2.0% constraint on the relative flux levels.

Results from the simultaneous application of the two constraints on the flux normalizations are summarized here:

$$\sigma^{\nu}/E = 0.676 \cdot 10^{-38}\,\text{cm}^2/\text{GeV}$$
$$\sigma^{\bar\nu}/E = 0.333 \cdot 10^{-38}\,\text{cm}^2/\text{GeV}. \tag{57}$$

The error on the cross section slope ratio was estimated at 1.7% while the overall, correlated error was estimated at 3.1%.

Acknowledgements. We are grateful for the skilled and dedicated efforts of the Fermilab staff, in particular, the Neutrino Crew members, and of many individuals at our home institutions. We thank Drs. K. Jenkins, R. Pitt, S. Pordes and D. Owen for their contributions to the flux monitoring. This research was supported by the National Science Foundation and the U.S. Department of Energy.

* While the z-resolution suffers at low E_{had}, the y-resolution is good

**These include primarily quasi-elastic scattering, resonance production and coherent pion production

References

1. G. Altarelli, G. Martinelli: Phys. Lett. 76B (1978) 89; M. Gluck, E. Reya: Nucl. Phys. B145 (1978) 24
2. D. Gross, F. Wilczek: Phys. Rev. Lett. 30 (1973) 1343; H. Politzer: Phys. Rev. Lett. 30 (1973) 1346
3. R. Blair et al.: NIM 226 (1984) 281
4. A. De Rújula, R. Petronzio, A. Savoy-Navarro: Nucl. Phys. B54 (1979) 393
5. P. Auchincloss, Ph.D. Thesis: Measurement of the cross section for charged-current neutrino-nucleon interactions, Columbia University (1986)
6. M. Purohit, Ph.D. Thesis: Nucleon structure from ν_μ-Fe interactions and a study of the valence quark-distribution, Caltech (1984)
7. D. Gross, C. Llewellyn-Smith: Nucl. Phys. B14 (1969) 337
8. G. Altarelli, G. Parisi: Nucl. Phys. B126 (1977) 298
9. D. MacFarlane et al.: Z. Phys. C - Particles and Fields 26 (1984) 1
10. B. Vallage, Ph.D. Thesis: Determination precise des fonctions de structure du nucleon dans les interactions de type courant-charge de neutrinos sur cible de Fer, Univ. Paris XI Orsey (1987)
11. F. Bergsma et al.: Phys. Lett. 123B (1983) 269
12. K. Varvell et al.: Z. Phys. C - Particles and Fields 36 (1987) 1
13. P. Meyers et al.: Phys. Rev. D34 (1986) 1265
14. J. Aubery et al.: Nucl. Phys. B272 (1986) 158
15. A. Benvenuti et al.: CERN-EP/87-100 (1987); A. Benvenuti et al.: Phys. Lett. 195B (1987) 91
16. L. Whitlow et al.: Univ. Rochester Report, UR1102 (1989)
17. W. Bardeen, A. Buras, D. Duke, T. Muta: Phys. Rev. D18 (1978) 3998
18. A. Devoto, D. Duke, J. Owens, R. Roberts: Phys. Rev. D27 (1983) 508
19. H. Georgi, D. Politzer: Phys. Rev. D9 (1974) 416; D. Gross, F. Wilczek: Phys. Rev. D9 (1974) 980
20. R. Barnett: Phys. Rev. D27 (1983) 98
21. A. Bodek, J. Ritchie: Phys. Rev. D23 (1981) 1070
22. H. Georgi, D. Politzer: Phys. Rev. D14 (1976) 1829
23. D. Duke, J. Owens: Phys. Rev. D30 (1984) 49
24. A. Benvenuti et al.: CERN-EP/89-06 (1989)
25. A. Benvenuti et al.: Phys. Lett. B195 (1987) 97; A. Benvenuti et al.: CERN-EP/89-07 (1989)
26. K. Lang et al.: Z. Phys. C - Particles and Fields 33 (1987) 483; C. Foudas et al.: Phys. Rev. Lett. 64 (1990) 1207
27. R.M. Barnett: Phys. Rev. Lett. 36 (1976) 1163; H. Georgi, H. Politzer: Phys. Rev. D14 (1976) 1829
28. R. Blair et al.: Phys. Rev. Lett. (1983) 343